

DR. CHARLOTTE GLADSTONE (Orcid ID : 0000-0001-8869-2520)

Article type : Original Manuscript

## The formation of convolute lamination in mud-rich turbidites

Gladstone, C.<sup>†</sup>, McClelland, H.M.O.<sup>^</sup>, Woodcock, N.H.\* , Pritchard, D<sup>‡</sup>. and Hunt, J.<sup>†</sup>

<sup>†</sup>BP Institute for Multiphase Flow, University of Cambridge, Madingley Road, Cambridge CB3 0EZ, UK

<sup>^</sup>Earth and Planetary Sciences Department, Washington University in St Louis, Campus Box 1169, 1 Brookings Drive, Saint Louis, MO 63130, USA.

\*Department of Earth Sciences, University of Cambridge, Downing Street, Cambridge CB2 3EQ, UK

<sup>‡</sup>Department of Mathematics and Statistics, University of Strathclyde, 26 Richmond Street, Glasgow G1 1XH, Scotland

<sup>†</sup>National Oceanography Centre, University of Southampton, Waterfront Campus, European Way, Southampton SO14 3ZH, UK

**Associate Editor – Jaco Baas**

### ABSTRACT

Convolute lamination is a common fold structure within turbidite beds, attributed to the deformation of sediment during or soon after deposition of the host bed. Despite the prevalence of this feature, the formational processes are still not well understood. Possible mechanisms are investigated here through redescription and analysis of convolute lamination from the Aberystwyth Grits Group (Silurian, west Wales, UK), in which ‘convolute bedding’ was first defined. Internal bed structures have been studied in clean coastal exposures and on high-resolution optical scans of cut surfaces. Convolute lamination occurs in intervals 2 to 10 cm thick, spanning the top of the very fine sand Bouma C division through the D division of interlaminated silt and clay. Observed growth geometries confirm that the structure formed during sedimentation of the host graded bed. Folds

This is an Accepted Article that has been peer-reviewed and approved for publication in the *Sedimentology*, but has yet to undergo copy-editing and proof correction. Please cite this article as an “Accepted Article”; doi: 10.1111/sed.12447

This article is protected by copyright. All rights reserved.

show a down-flow asymmetry and doubly-vergent diapiric geometries ('mushroom'-shaped structures). Grain size measurements from a modern turbidite (Icod bed, *ca* 165 ka, Moroccan Turbidite System) suggest that there is an optimal 'window' of average grain size and mud content parameter space, within which convolute lamination develops. It is proposed that this window coincides with a bed density inversion created during deposition of a graded bed as clean sand (with pore spaces infilled by water) fines upwards into mud-rich sand (with pores infilled by an increasing proportion of mud). Porosity decreases and bulk bed density correspondingly increases. The resulting unstable density gradient may lead to vertical buoyancy-driven overturn, manifest as growing folds. Subsequent amplification of the folds due to density differences and modification due to horizontal shear imposed by the depositing turbidity current may then occur. The bed density gradient stabilises with deposition of low permeability mud, suppressing further fold development. Quantitatively, both Rayleigh-Taylor instability and Kelvin-Helmholtz instability are theoretically possible in forming folds in this context.

Corresponding author: C Gladstone [lotty@bpi.cam.ac.uk]

Running title: Convolute lamination in mud-rich turbidites

Keywords: Aberystwyth Grits Group, convolute lamination, hydrodynamic instability, Icod bed, Moroccan Turbidite System, soft sediment deformation, turbidite

## INTRODUCTION

Convolute lamination is a fold structure confined within a single bed (Fig. 1) rather than involving a number of beds. The structure is therefore thought to form during or soon after deposition of the host bed. Although first defined in turbidite beds, the term convolute lamination has been extended to other depositional environments, not the focus of the present paper.

Proposed formation mechanisms for convolute lamination in turbidites include shear by the turbidity flow, shear due to a depositional slope, buoyancy instability and water escape (Allen, 1985). However, there is no consensus on the relative importance of these mechanisms. This paper clarifies possible mechanisms by re-describing and re-interpreting the type convolute lamination, defined by Kuenen (1953) in the Aberystwyth Grits Group of west Wales, UK. Field observations are coupled with grading measurements through an analogous turbidite containing convolute lamination, the Middle Pleistocene Icod event within the Moroccan Turbidite System, offshore north-west Africa. Three possible hydrodynamic mechanisms are then assessed quantitatively, by exploring the likely physical state of the sediment and the depositing flow at the time of deformation, and using these to estimate the growth of instabilities. A hypothesis is proposed for the development of convolute lamination in deep-marine turbidites. A better understanding of this

structure allows its more effective use in facies and palaeoflow analysis and informs the debate on triggers for soft-sediment deformation (Owen *et al.*, 2011).

### **DEFINITION OF CONVOLUTE LAMINATION**

Although convolute lamination was occasionally described under other names early in the 20th Century (e.g. Fearnside, 1910; Jones & Pugh, 1935), it only became commonly recorded with the upsurge of interest in graded bedding around 1950 (Migliorini, 1950; Rich, 1950; Natland & Kuenen, 1951). The structure was most fully described, and named as 'convolute bedding', by Kuenen (1953) using examples from the turbidites of the Aberystwyth Grits. The main features of the Kuenen definition were (Fig. 2A):

- deformation is contained within one graded bed, with only one fold zone within each bed;
- fold amplitude decreases both upward and downward from near the centre of the deformed zone;
- the top of the convolute zone may or may not be eroded and overlain unconformably by finer sediment;
- the bed boundaries are unaffected by folding and the bed maintains the same thickness laterally;
- no rupture of the laminae occurs;
- deformation is apparent in two planes at right angles to one another.

The definition by Kuenen has stood the test of time, although further characteristic features have been added (Allen, 1985):

- convolute anticlines tend to be tighter than the synclines;
- folds tend to be double-hinged and to develop elastica ('mushroom') shapes;
- individual laminae tend to thicken and thin from one part of a fold to another.

Allen (1977; 1985) also formalised Kuenen's recognition of internal discordances into three kinematic categories (Fig. 2B): (i) *post-depositional* if the bed has no internal discordances; (ii) *meta-depositional* if laminae are truncated at the top of the convolute zone; (iii) and *syn-depositional* if laminae are truncated within the deformed zone. This distinction is valuable in diagnosing formation mechanisms.

## FORMATION MECHANISMS FOR CONVOLUTE LAMINATION

All hypotheses for forming convolute lamination require unconsolidated sediment during deformation. Moreover, the sediment must have behaved in a plastic manner in which some or all of the weight of the grains was supported by the interstitial fluid. Even before ‘convolute lamination’ was named, it was recognised that this ‘hydroplasticity’ in graded beds might arise during sedimentation (Challinor, 1949; Migliorini, 1950), or during post-depositional compaction (Rich, 1950), or by seismic triggering (Bailey, 1930; Jones, 1938). Because the convolutions of the Aberystwyth Grits evidently formed during deposition of the host bed, the emphasis in this paper is on the first of these causes – sedimentation – whilst not precluding post-depositional causes in other environments (e.g. Owen *et al.*, 2011). Early authors (e.g. Kuenen & Migliorini, 1950; Ten Haaf, 1956) also recognised that well-sorted sands are too permeable to retain water during sedimentation, and that silt and clay must be present to reduce permeability and suppress vertical fluid flow. Fine sediment has a yield stress, above which it behaves as a viscous fluid and below which it behaves as an elastic solid. In subsequent discussions of mechanics, the sediment is assumed to be above the yield point, so within the kinematic boundary layer of Butler *et al.* (2016). Below the yield surface, the deposit behaves as a solid.

Four main deforming mechanisms have been proposed (Fig. 3) that could act individually or combine to produce convolute lamination.

*Downslope shear* (Fig. 3A) was proposed by Rich (1950) based primarily on observations from the Aberystwyth Grits. Rich (1950) envisaged each graded bed being sedimented on a basin slope, buried by later beds, fluidized by throughflow of compaction water, then acting as a ductile horizon on which higher sediments crept downslope. Williams (1960) proposed that heterogeneous folding arose from patchy distribution of liquefied sediment within the bed. Dżułyński *et al.* (1959) and Nagtegaal (1963) suggested that gravity-induced downslope shear could just as well operate at the sediment surface as at depth.

*Current shear* (Fig. 3B) was suggested as a deformation mechanism by Kuenen (1953), again based mainly on Aberystwyth Grits examples. Kuenen (1953) argued that deformation occurred close to the depositional surface because: (i) convolute troughs are filled by cross-laminated silt; (ii) laminae thin over anticlines; and (iii) developing folds are eroded within the bed. Kuenen (1953) noted the close association between the folds and underlying ripples; and envisaged the convolutions growing by: “pressure....exerted by the water in the troughs and suction on the ridges....in the same manner as wind blowing over waves”. This hypothesis was developed by Ten Haaf (1956) using examples from the Italian Apennine Mountains and supported by other studies over the following decade (Dżułyński *et al.*, 1959; Holland, 1959; Sanders, 1960; Dott & Howard, 1962; Dżułyński & Smith, 1963).

*Buoyancy instability* (Fig. 3C) was considered as a mechanism for convoluted deformation by Natland & Kuenen (1951), but with no proposal for generating the necessary inverse density gradient. Sullwold (1959; 1960) proposed an involved hypothesis that buoyancy-induced load structures at the base of graded beds might be re-eroded, then be draped by sediment that mimicked convolute lamination. Dżułyński & Smith (1963) suggested a simpler direct link between loading of sand on mud at the base of a bed and the formation of convolute lamination within it. Experimental studies (Dżułyński, 1966; Anketell & Dżułyński, 1968; Anketell *et al.*, 1970) then clarified that load structures at an inverse-density interface have polygonal patterns in the absence of shear on the bed, but more aligned patterns where the bed is sheared. Allen (1977) showed that a reverse density gradient can be produced by liquidizing a normally graded layer and letting it settle, with the larger, lower grains falling faster than the smaller higher grains to produce a packing gradient. This effect could happen during sedimentation as well as post-depositionally. Subsequently, Visher & Cunningham (1981) produced a theoretical model of Rayleigh-Taylor instability in reverse density sequences induced by fluidization, suggesting that it may apply to convolute lamination.

*Fluid escape* (Fig. 3D) has infrequently been invoked to explain convolute lamination in graded beds. Migliorini (1950) applied this mechanism to convolutions overlying tubular structures and Ten Haaf (1956) and Dott & Howard (1962) concluded that fluid escape would enhance the formation of anticlines formed by other mechanisms. Frey *et al.* (2009) showed experimentally how water-escape and gas-escape structures might be distinguished, although neither geometry matches turbidite convolute lamination.

## **GEOLOGICAL SETTING OF THE ABERYSTWYTH GRITS GROUP**

The Aberystwyth Grits Group, previously termed the Aberystwyth Grits Formation, is a Llandovery (early Silurian) turbidite system in west central Wales (Fig. 4). In common with several previous authors (e.g. Wood & Smith, 1958), the Aberystwyth Grits Group is referred to throughout this manuscript as the Aberystwyth Grits, for brevity. It is best observed in coastal cliffs between New Quay and Borth but is also exposed inland as far as the north-east-striking Bronnant Fault, which bounded the Aberystwyth Grits sub-basin to the south-east (Wilson *et al.*, 1992). The turbidity currents were confined within a linear upper crustal fault trough, during a transtensional phase of the Welsh Basin (review by Cherns *et al.*, 2006).

Terrigenous clastic material was supplied to the sub-basin mainly from the south-west. Data from erosional flutes and grooves (Wood & Smith, 1958) show that the turbidity currents flowed north-eastward along the axis of the sub-basin (Fig. 4). Average grain size and bed thickness decrease both north-eastward down the sub-basin and stratigraphically upward, from the coarser Mynydd Bach Formation to the finer Trefechan Formation. Ripple cross-lamination also shows flow mainly to the north-east (Wood & Smith, 1958) although there are two areas with anomalous directions; north-westerly flow near New Quay (Anketell & Lovell, 1976), and south-westerly flow

south of Borth (McCann & Pickering, 1989). All of the observations for the present study come from between these two anomalous sections, in the medial to distal parts of the system (Fig. 4).

### **HOST BED CHARACTERISTICS FOR CONVOLUTE LAMINATION**

Convolute lamination is most abundant in the upper unit of the Aberystwyth Grits – the Trefechan Formation (Fig. 1). This unit comprises thin to medium bedded sandstone–mudstone couplets (e.g. beds 3 and 7; Fig. 1) interbedded with very thin to medium bedded siltstone–mudstone couplets (e.g. beds 2, 4, 5, 6 and 8; Fig. 1). The sandstone percentage varies from 60% proximally to 30% distally (Lovell, 1970). The lower unit of the Aberystwyth Grits – the Mynydd Bach Formation – contains fewer siltstone–mudstone units and has additional sandstone beds up to 1 m thick, with basal grain size up to medium sand.

McClelland *et al.* (2011) logged a section of about 650 beds, mainly from the Trefechan Formation. These authors showed that convolute lamination rarely occurs in beds where the sandstone–siltstone interval is very thin (<30 mm). Rather, it is most common (111 beds) in thin to medium bedded sandstone–siltstone intervals (30 to 200 mm; e.g. beds 3 and 7; Fig. 1). Whatever the thickness of the host bed, the convoluted interval itself is always between 20 mm and 150 mm thick and is typically between 30 mm and 100 mm (McClelland *et al.*, 2011). This small range of convolute interval thickness presumably reflects a critical window of conditions (e.g. rheology, density and cohesion) during deposition, controlled by factors such as grain size, permeability and sedimentation rate.

Convolute lamination affects mainly the interlaminated silt and clay interval that, in non-convolute beds, is parallel laminated and part of the Bouma D interval (Fig. 5). Folding may affect the top of the underlying fine sand cross-laminated Bouma C division and McClelland *et al.* (2011) argued for Kuenen's (1953) hypothesis that folding nucleates on the crests and troughs of ripples in the C division. The amplitude of folding decreases rapidly towards the top of the laminated D division and affects the boundary with the overlying weakly or non-laminated mudstone of the Bouma E division. This E division is distinct from the infrequent very thin interturbidite intervals of hemipelagic laminated or burrowed mudstone (Davies *et al.*, 1997).

### **CONVOLUTE LAMINATION GEOMETRY**

Most outcrop-scale views of the Aberystwyth Grits convolute lamination (e.g. Fig. 1) confirm three key observations of Kuenen (1953): (i) folds occur within beds that show no folding of the bed boundaries; (ii) each bed contains only one zone of folds; and (iii) the fold amplitude is greatest in the centre of the convoluted zone and decreases towards the bed boundaries.

Scans of polished surfaces (Fig. 5) reveal more subtle fold geometries.

a) Convolute anticlines tend to lie above the crests of ripples in the cross-laminated sand and synclines above the ripple troughs (Fig. 5C). This correlation was observed by Kuenen (1953) and confirmed by McClelland *et al.* (2011). It suggests that *convolute folds nucleate on underlying current ripples*.

b) Folding is evident on any section through a convoluted bed, and must therefore be non-cylindroidal. McClelland *et al.* (2011, Fig. 12) identified the complex dome and basin patterns that the folded laminae make on horizontal bed surfaces. They suggested that *the non-cylindroidal folds nucleate on sinuous or linguoid ripples*.

c) In sections cut parallel to the local palaeoflow direction, fold axial planes are typically inclined down-flow (Fig. 5A). In sections cut perpendicular or oblique to the palaeoflow direction, folds tend to be more upright and symmetrical (Figs 5C and D). This down-flow inclination of folds suggests that *one component in fold formation is the bed shear stress imposed by the turbidity flow*.

d) Folds tend not to be simple structures with single hinges and axial surfaces. They develop double-hinged 'box-fold' geometries with opposing axial plane dips, then elastica 'mushroom' shapes (Ramsey & Huber, 1987) in which the limbs dip into, rather than away from, the fold core (Fig. 5C and D). The cores of the tighter elastica folds contain the closed lamination patterns called eye folds, particularly in sections perpendicular to current flow. McClelland *et al.* (2011) deduced that *the elasticas and eye folds develop from current-induced shear strains acting on already non-cylindroidal convolutions*.

e) Folded laminae typically include angular erosional discontinuities separating discordant sequences of lamination or cross-lamination (e.g. Fig. 5B). These 'sequence boundaries' may pass laterally into concordant sequences. Crucially, the sequence boundaries are themselves folded. These patterns were first recognised by Kuenen (1953, fig. 8) as typical 'growth geometries'; they imply that *the convolute folds amplified progressively during the sedimentation of the laminated silt-clay division rather than after the whole bed had been deposited*.

f) The folds include some volumes, always in the cores of anticlines, where the lamination in very fine-sand is disorganized or even homogenized (Fig. 5A, C and D). These volumes suggest that *the very fine sand was locally fluidized as pore water tried to escape upwards through the bed*.

g) Despite the evidence for fluidization, no examples of water-escape structures have been found, such as breached laminae, escape pipes or sand volcanoes. However, anticline crests tend to be flat-topped and their contained laminae to be conspicuously thinner than the same laminae in adjacent synclines. This thickness variation is partly due to preferential syndepositional ponding of sediment in the synclines. However, the tendency of extreme thinning of laminae to occur above volumes of disorganized sand suggests that *fluidized sand tended to rise buoyantly and pond below less permeable laminated silt and clay*.

In summary, the convolutions in the Aberystwyth Grits are associated with underlying ripples within the host bed. They are affected by downstream shear, and also by porosity and permeability changes within the bed that promote local fluidization while confining deformation by way of an impermeable cap. As grain size likely plays a controlling role on porosity and permeability, grain-size trends and sand to mud ratios are explored in the next section.

## **GRAIN-SIZE TRENDS**

### **Observations from the Aberystwyth Grits**

Hand-lens observations in the field (Fig. 1) and polished hand specimen scans (Figs 5 and 7) suggest that grain size is a key control on the formation of convolutions: lighter-coloured relatively clean sand underlies the folds, while dark-coloured sand-deficient sediment overlies the folds (Fig. 5A, C and D). The convolutions themselves consist of *ca* 1 mm thick graded sand/mud laminations (Fig. 6). Sediment is largely detrital quartz within a mud matrix, with larger stacked chlorite-mica grains replacing the altered fine fraction (Dimberline, 1986; Merriman, 2006) (Fig 6).

A block from Allt Wen (SN 576 797, sample X6) cut parallel to the palaeoflow was polished and thin-sectioned through the convoluted region (Fig. 7). The sediment underlying the folds (Fig. 7Ai and 7Cii) is pale, clean quartz from coarse silt to very fine sand (32 to 125  $\mu\text{m}$ ;  $5\phi$  to  $3\phi$ ). Within the convolutions, the coarser quartz grains are lost so the average grain size decreases to fine to medium silt (Fig. 7Aii, 7Aiii and 7Aiv) and, evident from the dark regions in the microscope images, the fines content is higher (Fig. 7Cii, 7Ciii and 7Civ). Dark structureless mud characterises the region above the convolutions (Figs 7Av and 7Cv). The folds in Figure 7 occur above Bouma C division and are capped by the structureless mud of the E division.

### **Observations from the Moroccan Turbidite System**

Unlithified sediments provide higher-quality quantitative grain-size information than ancient low-grade metasedimentary rocks such as the Aberystwyth Grits. Grain-size analysis was therefore done on an analogous muddy turbidite from the Moroccan Turbidite System of the Middle Pleistocene.

#### *Field area*

The Moroccan Turbidite System (MTS) is a series of intraslope basins and canyons leading from offshore north-west Africa shelf to the abyssal plain (Wynn *et al.* 2002). The area has been cored extensively and many beds named and cross-correlated from source to sink and between depositional basins (Fig. 8). Several beds exhibit convolute lamination; considered here is the Icod event turbidite (Bed 14 within the Agadir Basin).



Bed 14 is a very large volcanoclastic turbidite now correlated with the Icod landslide and associated debris flow, caused by the collapse of the north-eastern flank of Tenerife *ca* 165 ka. The flow not only deposited 22 km<sup>3</sup> of sediment as Bed 14 in the Agadir Basin but travelled west to deposit bed *g* (70 km<sup>3</sup>) in the Madeira Abyssal Plain and overspilled east to deposit bed *m* (13km<sup>3</sup>) in the Seine Abyssal Plain (Frenz *et al.* 2009).

Hunt *et al.* (2011) used geochemical and petrological techniques to show that Bed 14 comprises seven subunits (Fig. 9). The basal subunit correlates with failure lowest on the Tenerife submarine slope, with overlying subunits sourced from successive retrogressive failures from progressively higher locations such that the upper four subunits were subaerially-derived. Very thin mud layers between each subunit probably represent several days' pause between successive failures (Hunt *et al.*, 2011). While most beds are siliciclastics sourced from the Moroccan shelf that travelled west through the Agadir Basin, the Icod event was sourced from the Canaries and flowed east, and thus upstream, through the Agadir Basin.

Convolute lamination occurs in subunits 2 and 3 (Fig. 10) in the form of folds (cores CD166/27, 29 and 31) and flat-topped elasticas (core CD166/33). Hunt *et al.* (2011) identified convolute lamination within the central region of subunits 2 and 3. In both examples, the convolutions are underlain by ripple cross-laminated Bouma C sand and overlain by planar laminated Bouma D silt (Fig. 9). Both in terms of the bounding sedimentology and the fold geometry, the convolute lamination here resembles that observed in the Aberystwyth Grits.

#### *Data collection and trends*

Samples of 1 cm<sup>3</sup> were extracted continuously from the base to the top of each core and *ca* 10,000 grains analysed using a Malvern Mastersizer (Malvern Instruments Limited, Worcestershire, UK) to generate a full distribution histogram with bin width of  $\frac{1}{4}\phi$ . Within core CD166/27, Bed 14 is 159 cm thick, with the seven subunits thinning upward from 25 cm (subunit 1) to 5 to 10 cm thick (subunits 5, 6 and 7). These are overlain by a thick 80 cm mudcap (Figs 9 and 10). Each subunit grades normally, with decreasing average grain size (Fig. 11A) and increasing proportion of fine grains,  $\Phi_F$  (Fig. 11B). For consistency with other MTS size analyses (e.g. Hunt *et al.* 2011, Stephenson *et al.* 2014), the upper boundary of the fine fraction is defined as 32  $\mu\text{m}$  ( $5\phi$ ), although Frenz *et al.* (2009) used a cut-off of 10  $\mu\text{m}$  ( $6.6\phi$ ). Four different measures of grain size can be evaluated (Fig. 11A): (i) volumetric mean,  $d_{vol}$ ; (ii) modal value,  $d_{mod}$ , (cf. Hunt *et al.* 2011, Stephenson *et al.* 2014); (iii) the 50<sup>th</sup> percentile,  $d_{50}$ , which yields values that track the mode but can be much smaller for the finer distributions; and (iv) the 90<sup>th</sup> percentile,  $d_{90}$ . This last measure is included because comparisons between measurements taken first by a hand lens and grain size comparator, and second using a Malvern (Sumner *et al.*, 2012), indicate that hand-specimen values correlate with the coarsest 5 to 20% of the full size distribution. The  $d_{90}$  value provides a link with field estimates in ancient systems. In subsequent figures,  $d_{50}$  is used because the presence of occasional coarse grains in the sediment, which will not feature in  $d_{mod}$ , may be important in terms of processes.

Figure 11 shows that subunits 2 and 3 broadly grade normally, but that  $d_{vol}$  (Fig. 11A) and  $\Phi_F$  (Fig. 11B) show perturbations in the upward-fining trend through the convolutions, i.e. the grading is no longer monotonic. While these perturbations might represent the migration of grains during deformation, they may simply be the result of local inversion of the lamination by the folding, particularly where the original lamination is preserved.  $\Phi_F$  increases markedly across the upper boundary of the convoluted region (Fig. 11B). (Data points at  $h = 34$  cm and 35 cm are unfortunately unavailable.)

Plotting  $\Phi_F$  against  $d_{vol}$  for each sample yields information that is independent of bed height or subunit: there is a ‘window’ of parameter space corresponding to  $d_{vol}$  ca 50 to 100  $\mu\text{m}$  and  $\Phi_F$  ca 10 to 30% within which convolute lamination develops (Fig. 12; large grey circles). While convolute lamination may develop outside this window, other structures are not observed within it. Cross-laminated Bouma C sediment (diagonal crosses) may be of the same mean grain size as the folded region but lacks the fines content; conversely, planar-laminated Bouma D sediment (small black circles) may have a similar average grain size but has a higher fines content (>30%). While  $d_{vol}$  is important,  $\Phi_F$  is a key indicator for convolute lamination.

Full grain-size curves taken just below the folds, through the folds and just above (Fig. 13), indicate that sand is present in all samples although the amount and peak grain size decrease moving upward out of the convolutions. Mud is particularly prevalent in the sediment above the convolutions with clay also present here. Note the inversion of two curves compared to a perfectly graded bed owing to the folding.

### *Statistical analyses*

Sorting,  $\sigma_1$ , can be assessed using percentiles from the grain-size distributions (Folk & Ward, 1957). The cross-laminated sands underlying convolutions are moderately well-sorted with consistent values of  $\sigma_1 \sim 1$  (Fig. 14A). Convoluted sediment is more poorly-sorted, marking the onset of mud deposition ( $1 < \sigma_1 < 2$ ). The laminated silt above the deformation is very poorly sorted ( $\sigma_1 \sim 1.75$ ) reflecting the marked increase in clay content noted from Fig. 13A. Indeed, independent of bed depth, subunit or Bouma division,  $\sigma_1$  correlates highly with  $\Phi_F$  ( $r = 0.95$ ) (Fig. 14B), but less so with  $d_{vol}$  ( $r = -0.85$ ) or  $d_{90}$  ( $r = -0.83$ ), an indication of the coarsest sediment present

Calculated skewness,  $sk_1$ , (Folk & Ward, 1957) shows that the entire sequence is strongly fine-skewed. However there is no correlation between skewness and any of the grain-size parameters measured, although each division appears to plot in a characteristic region of parameter space (Fig. 15).

### *Summary of Icod grain-size analysis*

The measurements from the Icod turbidite core CD166/27 suggest that grain size is a key controlling parameter in the formation of convolute lamination, in particular the fines content and its control on sorting. Each division has characteristic sediment properties (Table 2):

- Bouma C sediment below the convolute lamination is moderately sorted, clean sand ( $\Phi_F < 15\%$ ) with  $d_{vol} \approx 100 \mu\text{m}$ .
- Convolute sediment is poorly sorted and contains more fines ( $\Phi_F = 10$  to  $40\%$ ) while retaining sand with  $d_{vol} \approx 80 \mu\text{m}$ .
- Overlying Bouma D laminated silt is very poorly sorted as  $\Phi_F > 50\%$  with prevalent clays, leading to a drop in average grain size,  $d_{vol} \approx 50 \mu\text{m}$ .

## QUANTITATIVE ANALYSIS OF CONVOLUTE LAMINATION FORMATION MECHANISMS

The underlying assumption of the following analysis is that convolutions arise because a perturbation nucleates on linguoid ripples (McClelland *et al.* 2011) and is amplified by some fluid-dynamical instability. First, estimates are obtained of the physical parameters that characterise the flow and the bed at the time of convolute lamination formation. These estimates are then employed to test the plausibility of proposed mechanisms, using results from linear stability analyses. Such analyses provide three main predictions: a stability criterion; a favoured wavelength,  $\lambda$ , or range of wavelengths for the perturbations that develop; and a growth rate  $\sigma$  for the early exponential phase of growth; in practical terms, the perturbation is expected to develop over several multiples of the timescale  $1/\sigma$ .

### Rough estimates of physical parameters

The following parameter estimates are arranged in decreasing order of reliability. Some (e.g. grain size and bed thickness) can be measured directly; others (e.g. Shields number) are estimated using measurements from other systems or laboratory evidence; and some (e.g. viscosity) are order-of-magnitude inferences. Values are summarised in Table 1.

The *density*,  $\rho_{bed}$ , of the newly-deposited bed can be estimated from the density of quartz ( $2650 \text{ kg m}^{-3}$ ), the density of water,  $\rho_0$  and plausible packing fractions  $\eta = 0.6 \pm 0.1$ , giving:

$$\rho_{bed} = \rho_0 + \eta(\rho_{qtz} - \rho_0) \approx (2000 \pm 200) \text{ kg m}^{-3}. \quad (1)$$

The *settling velocity*,  $w_s$ , of the grains can be estimated from the *grain diameter*,  $d$ , typically in the range (10 to  $100 \mu\text{m}$ ); allowing for the flocculation of clay, this suggests  $w_s$ , in the range ( $10^{-4}$  to  $10^{-3} \text{ m s}^{-1}$ ) (Allen, 1985).

The *deposition time*,  $T_{dep}$ , for the sediment layer that will subsequently be deformed can be estimated by considering the depositional flux. The downward volume flux of sediment per unit area is  $w_s C$ , where  $C$  is the volume fraction of sediment in suspension; the time taken to build up a layer of thickness  $h$  is therefore:

$$T_{dep} = \frac{h\eta}{w_s C} \quad (2)$$

where a single value of  $h \approx 0.05$  m is typical for a convoluted layer from the Aberystwyth Grits, and values of  $C$  in the range 0.05 to 0.1 are plausible for turbidity currents (Mulder & Alexander, 2001), giving  $T_{dep} \approx (300 - 6000)$  s.

The *current speed*,  $U$ , and the closely-associated *bed shear stress*,  $\tau$ , play important roles in this parameter estimation and the instability criteria. Unfortunately, they are not straightforward to estimate, in part because of the need to separate the various drag components. Kuenen (1953), assessing the viability of his proposed mechanism, uses a current speed of  $0.6 \text{ ms}^{-1}$  although that study also uses observations of current ripples to estimate that: “the bed velocity at a certain point may first be too high for rippling, probably more than 50 cm per second. As the velocity decreases rippling starts, attains a maximum and then falls off again. By the time the tail of the turbidity current is passing the point in question at a velocity below 25 cm per second, rippling stops and the top of the bed is deposited in parallel flat laminae.” This suggests that the convolute lamination formed under current speeds rather lower than Kuenen (1953) uses in the assessment of the mechanism.

Rather than estimating  $U$  a priori, a value is inferred directly from sedimentological evidence. It is necessary to distinguish between the *skin drag* felt as stress on the bed, and the *total drag* which includes contributions from form drag,  $c_f$ , and from the upper interface of the current  $c_i$ :

$$\tau = c_s \rho_C U^2 \quad \text{and} \quad \tau_{tot} = c_{tot} \rho_C U^2 \quad (3)$$

where  $\tau$  is the stress felt by the bed as skin drag,  $c_{tot} = c_s + c_f + c_i$ , and  $\rho_C$  is the density of the current. The skin drag is the relevant quantity both for the Shields diagram and for the viscous deformation of the freshly-deposited bed.

The Shields number  $\Theta$  must first be estimated; from this  $\tau$  is evaluated and  $U$  obtained via a Chezy drag law:

$$U = \left( \frac{\tau}{c_s \rho_C} \right)^{1/2} \quad (4)$$

[The skin drag rather than total drag is used in Eq. 4; this concurs with the basic physics of sediment motion (e.g. Dyer, 1986) but Leeder (1982) suggests that total drag is often used.] Typical *Shields numbers*,  $\Theta$ , exerted by the turbidity current on the recently-deposited bed are estimated from the region of the Shields diagram (e.g. Allen, 1985) in which the sedimentary structures appear. The deformed interval occurs once the current has waned just past the ripple stage, where the Shields parameter,

$$\Theta = \frac{\tau}{\rho_0 g' d} \quad (5)$$

is of the order of 0.03 to 0.1 for non-cohesive sediment, and  $g'$  is the reduced gravity driving the flow. Recent work on the development of bedforms using cohesive sediment suggests that, for mud-

rich beds such as the Aberystwyth Grits or the Icod turbidite, a value of  $\Theta \approx 1$  may be appropriate (Baas *et al.*, 2016). Given  $\Theta$ , typical bed shear stresses  $\tau$  exerted by the turbidity current on the recently-deposited bed can be estimated. Taking  $g' = 1.65g$  and a representative grain size  $d_{\text{typ}} \approx 3 \times 10^{-5}$  m for the mixed-grain-size bed, gives  $\tau \approx (0.015 - 0.05)$  Pa.

Unfortunately, there is considerable uncertainty in the drag coefficients  $c_s$  and  $c_{\text{tot}}$  for turbidity currents. Garcia & Parker (1993) found  $c_{\text{tot}}$  of the order of 0.03 to 0.09. These authors also found that the skin friction coefficient  $c_s$  was a decreasing function of Reynolds number, between 0.01 and 0.04 for most of the experiments, and that form drag was dominant for flow over erodible beds on which bedforms developed. Kneller & Buckee (2000) quote work suggesting that  $c_i > c_s + c_f$  and that  $8c_{\text{tot}} \approx 0.01$ , i.e.  $c_{\text{tot}} \approx 0.00125$ . This expression agrees to within about 20% with the observed current speed quoted by Middleton (1993) for turbidity currents in Sanmenxia reservoir. Srivatsan *et al.* (2004) used a value of  $c_{\text{tot}} = 0.005$ . Most recently, Sequeiros *et al.* (2010) found effective basal drag coefficients  $c_s + c_f$  of the order of 0.01 for currents that are deep relative to the vertical scale of bedforms. [The field-scale data presented in fig. 21 of Sequeiros *et al.* (2010) include the effect of dunes a metre or more in amplitude, and fig. 15 suggests skin drag only an order-unity factor smaller than the total basal drag.] Here, values for  $c_s$  in the range  $10^{-3}$  to  $10^{-2}$  and  $c_{\text{tot}}$  a factor of two to five higher are used, so as to be reasonably confident of bracketing the correct values of  $U$ .

Given  $\tau$ , and applying the estimates of  $c_s$ , the *current speed*,  $U$ , is estimated from Eq. 4 as  $(0.04 - 0.5)$  m s<sup>-1</sup>. It is reassuring to note that this estimate is similar to the independently-obtained value from Keunen (1953).

Finally, some tentative estimates of the *viscosity*,  $\mu$ , of the recently-deposited bed may be made by assuming that this bed behaves as a Newtonian fluid, and that the downstream overturning of structures is driven principally by the imposed shear. Typically, structures are deformed with an aspect ratio of about one, suggesting that the top of the bed has travelled roughly  $h$  downstream while the bed thickness  $h$  was being built up vertically. Assuming that this occurred over the timescale  $T_{\text{dep}}$ , the typical shear rate  $\dot{\gamma}$  can be estimated as:

$$\dot{\gamma} \approx \left(\frac{1}{h}\right) \left(\frac{h}{T_{\text{dep}}}\right) = \frac{1}{T_{\text{dep}}} . \quad (6)$$

This shear must be driven by the shear stress imposed at the bed, so:

$$\tau = \mu \dot{\gamma} \quad \text{i.e.} \quad \mu \approx \tau T_{\text{dep}} \quad (7)$$

giving an estimate for  $\mu$  in the range  $(4.5 - 300)$  Pa s. The lower end is about 5000 times the viscosity of water, placing it only an order of magnitude higher than the Bingham viscosities reported elsewhere for fluid mud (Mei *et al.*, 2001). Given the extreme uncertainties in measuring or inferring the rheology of dense suspensions, even this level of agreement is encouraging. (Note also that fitting a Bingham model to a given fluid gives lower viscosities than fitting a Newtonian model, because some of the stress in the Bingham model must be accommodated by the plasticity.)

Table 1 summarises the reconstructed parameter values for use in the subsequent assessment of instability mechanisms. No accuracy greater than order of magnitude is implied for any of the inferred quantities. As a check, the Reynolds number:

$$\text{Re} = \frac{\rho_c U H}{\mu} \quad (8)$$

can be estimated. For a conservatively thin current of depth  $H = 1$  m, minimum density  $1000 \text{ kg m}^{-3}$  and viscosity  $10^{-3} \text{ Pa s}$ ,  $\text{Re} \sim (40,000 - 500,000)$  for the range of  $U = (0.04 - 0.5) \text{ m s}^{-1}$ . These values are comfortably within the turbulent regime. Evidence from natural flows suggests  $H \gg 1$  m (e.g. Sumner and Paull, 2014), giving  $\text{Re} \sim (10^6 - 10^7)$ .

### Instability mechanisms

To be considered a plausible candidate for the generation of convolute lamination, an instability mechanism should satisfy three criteria:

- (i) Perturbations of the observed wavelengths ( $\lambda \approx 0.1$  m) are unstable in a parameter regime consistent with the estimates above. This is necessary for the instability to nucleate on the underlying ripples as observed. If the preferred wavelength of instability is very different from the ripple wavelength, this close correlation is unlikely to develop.
- (ii) Perturbations can develop on a timescale comparable with  $T_{\text{dep}}$ . (Much slower processes will be unable to distort the laminae significantly; much faster ones should fully develop long before the bed has formed, and should thus form features at a smaller vertical scale.)
- (iii) There should be some reason why the instability is not observed in the overlying or underlying regions of the deposit.

It should be noted at the outset that the instability criteria and the instability growth rates are obtained from strongly idealised models and are indicative: like the parameter reconstruction above, the quantitative reasoning that follows is order of magnitude only.

#### *Syn-depositional shear (Fig. 16A)*

Kuenen (1953) proposed a mechanism, akin to the Kelvin-Helmholtz instability (Drazin, 2002), in which the deformation of the bed was driven by pressure variations in the overlying flow, due to the acceleration and deceleration of the flow over the rippled bed (Fig. 16A). An analysis is given in the Appendix; the instability criterion, in terms of wavenumber  $k$ , and current velocity  $U$ , is:

$$k > k_{\text{cut}} = \frac{g(\rho_{\text{bed}} - \rho_c)}{\rho_c U^2} \quad (9)$$

while the growth rate  $\sigma$  of perturbations is generally of the order of:

$$\sigma \leq \frac{\rho_C U^2}{2\mu} \quad (10)$$

being significantly smaller than this only very close to the threshold of instability. (Note that the viscosity  $\mu$  modifies the growth rate but not the stability criterion.) The current density,  $\rho_C$ , is given by:

$$\rho_C = \rho_0 + C(\rho_{qtz} - \rho_0) \approx 1200 \text{kgm}^{-3}. \quad (11)$$

Estimates for  $\rho_{bed}$ ,  $U$  and  $\mu$  have already been obtained; the estimates for  $U$  and  $\mu$  are not independent so  $U^2/\mu$  must be calculated as a single cluster. Employing the estimated values for  $U$  (Table 1) yields:

$$20 \text{m}^{-1} \leq k_{cut} \leq 5000 \text{m}^{-1}, \quad \text{i.e. } 0.001 \text{m} \leq \lambda_{cut} \leq 0.30 \text{m}. \quad (12)$$

There is significant uncertainty due to the range of  $U$ , but it appears that the imposed wavelengths of order 0.1 m are narrowly within the unstable range. If instead Keunen's (1953) value  $U = 0.6 \text{m s}^{-1}$  is used,  $k_{cut} \approx 18 \text{m}^{-1}$  and thus the cutoff wavelength is slightly higher,  $\lambda_{cut} \approx 0.34 \text{m}$ . This implies that syn-depositional shear is plausible, particularly if the current velocity within this discussion has been underestimated.

Rewriting the estimate for  $\sigma$  in terms of more directly measured or inferred quantities gives:

$$\sigma \leq \frac{1}{2} \rho_C \frac{U^2}{\mu} = \frac{\rho_C}{2c_s \rho_0} \frac{1}{T_{dep}} \quad (13)$$

Taking the lower and upper estimates of  $c_s$  yields:

$$\frac{60}{T_{dep}} \leq \sigma \leq \frac{600}{T_{dep}}, \quad \text{i.e. } \frac{T_{dep}}{600} \leq T \leq \frac{T_{dep}}{60} \quad (14)$$

These estimates give a characteristic time for the instability which is at least an order of magnitude shorter than the time for the bed to form. Although larger estimates of  $c_s$  would lead to smaller estimates of  $U$ , and thus to slower growth, they would also lead to smaller cut-off wavenumbers. The instability would then be unable to nucleate on the underlying ripples because these have a larger wavelength of around 10 cm.

### Buoyancy-driven Rayleigh-Taylor instability (Fig. 16B)

The second hypothesis to be assessed is that convolute lamination is due to a buoyancy-driven instability akin to the Rayleigh-Taylor instability (see e.g. Drazin, 2002, §3.7; Chandrasekar, 1961). This builds on work by Anketell & Dżułyński (1968), Anketell *et al.* (1970), Allen (1977) and McClelland *et al.* (2011).

Following Conrad & Molnar (1997, §5.3), the instability of a layer of depth  $h$  with an unstable density contrast  $\rho_1 - \rho_2$  across it, overlying an infinitely deep layer of constant density  $\rho_2$ , is considered (Fig. 16B). There is no effective mechanism to prevent gravitational instability; viscosity merely influences the growth rate and wavelength selection. The viscosity of the lower layer has only a weak effect on the dominant mode of instability (Conrad & Molnar, 1997), so for simplicity both layers are assumed to have viscosity  $\mu$ .

Results from Conrad & Molnar (1997) for the most rapidly growing perturbation are:

$$k \approx \frac{2}{h}, \quad \sigma \approx 0.04 \frac{(\rho_1 - \rho_2)gh}{\mu_1} = 0.04 \frac{(\rho_1 - \rho_2)gh}{\tau T_{dep}} \quad (15)$$

In contrast to the syn-depositional shear mechanism, there is no cut-off wavenumber for the buoyancy-driven instability to occur.

An upper bound on the density contrasts of the order of  $\rho_1 - \rho_2 \approx 200 \text{ kg m}^{-3}$  is estimated; a discussion as to the origin and magnitude of this density contrast is given in the subsequent section. Using the values in Table 1, estimates of the favoured wavenumber  $k$  and the growth rate  $\sigma$ , are thus obtained:

$$k \approx 40 \text{ m}^{-1}, \quad \frac{8}{T_{dep}} \lesssim \sigma \lesssim \frac{270}{T_{dep}} \quad (16)$$

These correspond to favoured wavelengths  $\lambda$  and growth timescales  $T$  in the range:

$$\lambda \approx 0.16 \text{ m} \quad \text{and} \quad \frac{T_{dep}}{270} \lesssim T \lesssim \frac{T_{dep}}{8} \quad (17)$$

The favoured wavelengths predicted by this analysis are close to that of the underlying ripples, suggesting that this mechanism might be effective. The growth rates are more problematic, because the timescale for the perturbations to develop remains an order of magnitude smaller than the deposition time for the convoluted portion of the bed. It is worth noting, however, that if the density contrast  $\rho_1 - \rho_2$  were rather smaller than the upper bound employed in these estimates,  $T$  would be proportionally increased. Likewise, if only a portion of the convoluted bed is unstably stratified then the effective value of  $h$  in the expression for  $\sigma$  is reduced, reducing both the growth rate and the wavelength. The subsequent discussion on packing and resulting bed density changes suggests that, indeed, only a small portion of the bed will experience a reverse density gradient.



Overall, these calculations suggest that the buoyancy-driven instability mechanism developed here using grain-size considerations is plausible, and although some problems remain, they are less pronounced than for the shear mechanism.

#### *Viscous buckling instability (Fig. 16D)*

The third hypothesis, which is less plausible as demonstrated below, is that shear in the cross-current direction, associated with the pattern of linguoid ripples on which the convolute lamination nucleates might trigger viscous buckling (Benjamin & Mullin, 1988) in a thin but highly viscous layer of recently deposited silt/mud (Fig. 16C). Viscous buckling is a three-dimensional process in which shear in the  $y$ -direction of a flow moving in the  $x$ -direction causes buckling in the  $z$ -direction.

The analysis by Benjamin & Mullin (1988) involves a thin, highly viscous layer of density  $\rho_1$  viscosity  $\mu$  and thickness  $h$  floating on an inviscid layer of density  $\rho_2 > \rho_1$ . To inherit this analysis, a partly fluidized sandy deposit may be treated as the supporting layer, and thus  $\rho_1 \approx \rho_2 \approx \rho_{bed}$ . Neglecting surface-tension, the stability criterion is:

$$S > S_c = \frac{g\rho_{bed}h}{2\mu} \min_{\gamma} \frac{\cosh^2(\gamma)}{\gamma^2} \approx 1.1 \frac{g\rho_{bed}h}{\mu} \quad (18)$$

where  $S$  is the horizontal shear rate. To obtain a lower estimate of  $S_c$  the largest estimate of  $\mu \approx 300$  Pa s is taken, which along with  $\rho_{bed} \approx 2000$  kg m<sup>-3</sup> and  $h \approx 0.05$  m gives  $S_c \gtrsim 0.3$  s<sup>-1</sup>. Meanwhile, an upper bound on  $S$  is  $S \lesssim U/L$ , where  $L$  is the cross-flow spacing of the linguoid ripples. With  $U \lesssim 0.5$  m s<sup>-1</sup> and  $L \gtrsim 0.1$  m, these give  $S \lesssim 5$  s<sup>-1</sup>. Taken together, these constraints make it just possible that horizontal shear rates sufficient to initiate the instability could occur in flow over ripples of the dimensions observed in the Aberystwyth Grits. The evidence thus suggests that viscous buckling is at best a marginally plausible explanation for the convolute lamination found within the Aberystwyth Grits, when the extreme estimates from Table 1 are used.

#### **Summary of analytical comparisons**

These analyses represent an attempt to compare different instability mechanisms using real parameters. It is possible that more refined mathematical models would yield quantitatively different predictions. Conclusions based on estimated values of  $U$  or  $\mu$  should be regarded with special caution. However, some progress in testing the candidate mechanisms against the three outlined criteria can be made.

Criterion (i), which relates to the allowed and favoured wavelengths of the instabilities, appears sufficient to rule out viscous buckling, while syn-depositional shear and buoyant overturn remain possible mechanisms. In both cases the preferred wavelength of the instability is close to that of the ripples, although it is rather closer for the buoyant than the shear mechanism.

Criterion (ii), which relates to the growth rate of perturbations, is problematic for both the shear-driven and buoyancy-driven mechanisms because the timescale over which the instability develops is shorter than the deposition time for the bed. This problem is more acute for the shear mechanism, for which the factors controlling the instability are more tightly constrained, than for the buoyancy-driven mechanism.

Finally, criterion (iii), which relates to the location of convolute lamination within the bed, tends to support the buoyancy-driven mechanism. This mechanism, which relies on local vertical density gradients, offers an explanation as to why convolute lamination should be associated with beds of a particular composition; the shear-driven mechanism is unable to explain this

## RELATIONS BETWEEN GRAIN SIZE AND BED DENSITY

In this section, the effect of grain size on packing and thus bed density is discussed, to explore the assertion that a normally-graded turbidite has the potential to be unstably stratified in density, in accord with the Rayleigh-Taylor instability.

The grain-size distribution of a sediment affects its bulk properties in non-linear and non-unique ways. The key properties relevant to the formation of convolute lamination are the *porosity*,  $\phi$ , and *permeability*,  $\kappa$ , the *packing fraction*,  $\eta$ , (volume fraction occupied by grains i.e.  $\eta = 1 - \phi$ ) and the *packing density*,  $\rho_{pack}$  (mass per unit volume occupied by grains). Related via the pore-filling fluid is the *bed density*,  $\rho_{bed}$  (Eq. 1). For a dry powder,  $\rho_{pack} = \rho_{bed}$ ; for a marine sediment, the brine, which may also contain suspended clays, is included.

A large body of work has shown that the packing density is a function of (among many parameters) grain-size distribution, particle shape, the nature of the packing and indirectly, the absolute grain size.

### Bidisperse mixtures

V-shaped cross-plots relating bulk and elastic properties of rocks are well known in both chemical engineering (Cumberland & Crawford, 1987) and geophysics (Dvorkin *et al.*, 2014). The V-shape (Fig. 17) results from *dispersed mixing* of particles of two distinctly different mean sizes so that the fine grains with diameter  $d_f$ , fill the pore space between the coarse grains,  $d_c$ . This infilling causes a dip in porosity and corresponding peak in packing density. Dispersed mixing is distinct from *laminar mixing*, where the grains segregate according to their size, creating laminations and, consequently, as the fines content increases, the porosity evolves linearly between the two end-member porosities of  $\phi_c$  and  $\phi_f$ .

Experiments on bimodal systems have validated the V-shape and its porosity minimum,  $\phi_{MIN}$ . For example, Marion *et al.* (1987, 1992) report a porosity minimum in natural sand-clay sediment occurring at 20 to 40 wt% clay (Fig. 17A) with a dependency on pressure. The porosity minimum is caused by changes in packing. *Ideal packing* in this context occurs when the fine grains are fully accommodated within the pore spaces so that the original packing of the coarse grains is undisturbed. The ratio of the two diameters is the key parameter that governs packing (McGeary, 1961) with a mixture close to ideal when  $d_C \gg d_F$ . Marion *et al.* (1992) assumed ideal packing in their theory because for the experiments,  $d_C/d_F \approx 50$ . However, the actual value of  $\phi_{MIN}$  is underpredicted and so the concept of *fractional packing* (Koltermann & Gorelick, 1995) was introduced to model the more realistic scenario where, although one type of packing might dominate, local regions of different packing may occur (Fig. 17A).

Yin *et al.* (1993) next defined a critical volumetric clay content,  $\Phi_{CRIT}$ . When  $\Phi_F < \Phi_{CRIT}$  the sediment is framework-supported (coarse-packed) with the clay fraction replacing pore fluid, causing an increase in the bulk modulus and decrease in porosity (Fig. 17B). When  $\Phi_F > \Phi_{CRIT}$  the sediment is matrix-supported (fine-packed) because the addition of more clay causes the sand grains to become separated, decreasing the bulk modulus and increasing porosity. Coarse grains now act as non-porous, impermeable 'baffles' (Esselburn *et al.*, 2011).

The porosity minimum,  $\phi_{MIN}$ , occurs at  $\Phi_{CRIT}$ . This point also corresponds to the transition in reservoir geology between a shaley sandstone and a sandy shale, with a peak in p-wave velocity (Avseth, 2010). It is recognised in many studies showing that a bed composed of a mixture of coarse and fine particles can have a lower porosity, and thus a higher density, than a monodisperse bed of either fine or coarse material (e.g. Sohn & Moreland 1968; Allen 1985, §2.8; Yu & Standish 1987; Pirmez *et al.*, 1997; Kamann *et al.* 2007; Esselburn *et al.* 2011).

### **Polydisperse mixtures**

Natural sediments tend to be continuous distributions with  $\phi$  depending on the complex geometry of the sediment, the shape of the grain-size distribution, the ratio of the grain sizes and the packing of individual grains. Key studies on polydisperse mixtures include early experiments by Furnas (1931), the effect of different distributions by Sohn & Moreland (1968), and modelling of the Furnas (1931) data by Brouwers (2006), which relates porosity to both the size ratio and the relative volumetric ratio of constituent grains (Fig. 17C). An alternative modelling approach involves fractal models to characterise the grain-size distribution (e.g. Arya & Paris, 1981; Ghanbarian-Alavijeh *et al.*, 2011). Here the medium-sized grains fit into the pore spaces between the coarsest grains, with smaller pores infilled by progressively-smaller grains.

The current understanding is that poorly-sorted sediment packs more closely than well-sorted sediment (e.g. Roger & Head, 1961), but the optimal blend of particle sizes to create the bed density maximum is not known. Consequently there is insufficient understanding to state, on the basis of grain-size data alone, what the original density of a bed is likely to have been.

### Reverse density gradient estimates

Upper bounds for the density differences that may arise within an unconsolidated sand-clay turbidite can be obtained by assuming that:

- (a) in a clean sand, the pore space is filled solely with water, giving a bulk density:

$$\rho_{clean-sand} = \rho_0 + \eta_{sand} (\rho_{qtz} - \rho_0) \quad (19a)$$

where  $\eta_{sand}$  is the packing fraction, i.e. the volumetric fraction of sand.

- (b) in a muddy sand, the pore space is filled solely with mud, giving a bulk density:

$$\rho_{muddy-sand} = \rho_0 + \eta_{sand} (\rho_{qtz} - \rho_{mud}) \quad (19b)$$

- (c) the bulk density of mud is intermediate between that of water and of clay particles:  $\rho_{mud} = \rho_0 +$

$$\eta_{clay} (\rho_{clay} - \rho_0) \quad (19c)$$

Taking  $\eta_{sand} \approx 0.6$ ,  $\rho_{clay} = \rho_{qtz} = 2650 \text{ kg m}^{-3}$  and  $\eta_{clay} \approx 0.4$  provides estimates for  $\rho_{clean-sand} \approx 1990 \text{ kg m}^{-3}$  and  $\rho_{muddy-sand} \approx 2250 \text{ kg m}^{-3}$  suggesting that an unstable density gradient is likely at some height within the bed as clean Bouma C sand gives way to mud-rich sand. A change in sorting (Fig. 14A) also points to an increase in bed density within the now-deformed region (c.f. Rogers & Head, 1960).

The estimate of  $\Delta\rho = (\rho_{muddy-sand} - \rho_{clean-sand}) \approx 260 \text{ kg m}^{-3}$  represents the extreme case, so a lower value of  $\Delta\rho \approx 200 \text{ kg m}^{-3}$  is used in Eq. 15. Taking this simple estimate further is problematic because calculations on bed density involve a ternary packing problem. For summary, core measurements for  $d_{vol}$  and  $\Phi_F$  using different upper bounds, are listed in Table 2. Considering  $\Phi_F < 8 \mu\text{m}$  because, for an equivalent bimodal mixture  $d_F \sim 0.1d_C$ :  $\Phi_F$  doubles between the Bouma C division and the convolutions, yet quadruples between the convolutions and draping laminated silt. Assuming that Bouma C is grain-supported, this first increase might be accommodated within the pores, reducing  $\phi$  and increasing  $\rho_{bed}$ . However, the substantial increase above the folds may cause the sediment to evolve to matrix-support, returning to a lower bed density but with a crucial associated drop in permeability. The present authors suggest that this transition occurred within the now-deformed region.

Given the uncertainties, a key part of the proposed instability mechanism here remains speculative. Nevertheless, it is likely that, when there is sufficient fine material in the bed, a porosity minimum and therefore reverse density gradient may form at a critical clay content. Buoyant instabilities during the settling of sand–mud suspensions were observed experimentally by Amy *et al.* (2006), although only in a regime with relatively high concentrations and an intermediate fraction

of mud (their regime III); at higher mud fractions, both buoyant instability and elutriation were suppressed.

## **CONCLUSIONS**

### **Key features of convolute lamination**

Field observations reveal the following features relevant to turbidite convolute lamination generally:

- Convolute lamination occurs in discrete intervals within graded turbidites; intervals with a limited range of thickness (mostly 20 to 100 mm) and grain size (very fine sand to interlaminated silt/clay) that imply a restricted window of optimal formation conditions.
- Observed growth geometries confirm that the structure formed during sedimentation of the host graded bed.
- Folds are seen to nucleate above current ripples in the very fine sand of the Bouma C division and to reach their greatest amplitude in the interlaminated silt and clay of the Bouma D division.
- Folds show both a down-flow asymmetry, presumably due to current shear stress, and doubly-vergent diapiric geometries, presumably due to bed-normal buoyancy forces.
- Thin-section images and grain-size profiles indicate that the host bed grades normally, with the sand upward-fining gently through the convolutions but the mud fraction increasing rapidly.

### **Quantitative assessment of mechanisms**

Quantitative analyses of three possible causal mechanisms, employing field values to constrain parameters used to estimate growth times and fold wavelengths, indicate that both buoyancy-driven instability in the z-direction and shear instability in the x-direction are possible, in accord with the field observations. Problematically, folding theoretically occurs on a shorter timescale than the estimated deposition time of the affected layer. Viscous buckling, requiring cross-flow y-direction forcing, is unlikely. Post-depositional mechanisms and water escape are excluded based on field evidence.

## **Idealised sequence**

Using grain-size and sorting measurements from core, field observations from outcrop and inferring bed density based on the discussions earlier, a vertical sequence through a muddy turbidite is sketched in Fig. 18, with grain diameters and fractions proportional to data (Fig. 12 and Table 2). Clean Bouma B sand occurs at the base. Moving upward through Bouma C rippled sand, and into the convolute lamination, the sands gently fine and the proportion of mud progressively increases. This causes the sorting to deteriorate with a likely decrease in porosity and corresponding increase in bed density, leading to the development of an unstable density gradient within the depositing bed. At some critical fines content and height, the grain-supported framework is envisaged as evolving into a matrix-supported framework, with the sediment above returning to a stable density gradient. Allen (1972, 1977) suggested that simply a change from ripple to plane bedding may result in sufficient density contrast to create instability, as could resedimentation of a liquefied sediment. In the new hypothesis, the density reversal is an inherent primary feature arising from the natural packing of grains during deposition of a normally-graded poorly-sorted bed. Finally, a Bouma D/E division drapes the folds. This clay-rich sediment is very poorly sorted so likely to have a low porosity and a very low permeability.

## **Process hypothesis**

Dynamically, a dilute turbidity current is envisaged, depositing clean rippled sand (Fig. 19, label '1') that grades upward into higher-density mud-rich sand. This reverse density gradient leads to buoyancy-driven vertical movement of material (Fig. 19, label '2'). Upwelling regions occur above the crests of underlying linguoid ripples. While these early symmetrical folds are nucleating and developing, laminated sediment continues to be laid down over the folds and into the troughs. The overriding depositing current imposes sufficient shear to amplify the fold growth in the downstream direction (Fig. 19, label '3'). Finally, with clay-rich silt aggrading the bed (Fig. 19, label '4'), further development of the convolutions is suppressed. Clay plays a critical role in the process. It reduces the permeability of the deforming sediment so creating a plastic material with a yield stress. It generates the density contrast required to drive the Rayleigh-Taylor instability. Finally, clay-rich laminated silt confines the convolutions to a thin layer within the host bed.

## **ACKNOWLEDGEMENTS**

We thank Keith Gray (University of Cambridge) for assistance with sample preparation. Helpful reviews by Geraint Owen and Rob Butler improved the presentation of the paper.

## NOMENCLATURE

---

$C_s, C_{tot}, C_f, C_i$	Skin drag, total drag, form drag, interfacial drag coefficients
$C$	Volumetric fraction (concentration) of sediment in fluid suspension
$d$	Grain diameter
$d_{typ}$	Typical grain diameter
$d_C, d_F$	Diameter of coarse grains/fine grains in a bimodal mixture
$d_{VOL}$	Volumetric mean grain size
$d_{MOD}$	Modal grain-size diameter
$d_{50}, d_{90}$	50 <sup>th</sup> /90 <sup>th</sup> percentile value of grain-size distribution
$g$	Acceleration due to gravity
$g'$	Reduced gravity of a flow
$h$	Bed or layer thickness
$H$	Flow thickness
$\eta$	Packing fraction (= $1 - \phi$ )
$\eta_{sand}, \eta_{clay}$	Packing fraction of sand / clay
$k$	Wave number
$k_{cut}$	Cut-off wave number
$L$	Cross-flow spacing of linguoid ripples
$r$	Correlation coefficient
Re	Reynolds number
$S$	Horizontal shear rate
$S_c$	Critical horizontal shear rate
$sk_1$	Skewness of a distribution
$T$	Growth time of instability
$T_{dep}$	Deposition time

$U$	Current speed
$w_s$	Settling velocity
$\dot{\gamma}$	Shear rate
$\lambda$	Wavelength
$\lambda_{cut}$	Critical wavelength
$K$	Permeability
$\mu$	Bed viscosity
$\rho_{bed}$	Density of the bed
$\rho_c$	Density of the current
$\rho_{clay}$	Density of clay
$\rho_{clean-sand}$	Density of clean sand
$\rho_{mud}$	Density of mud
$\rho_{muddy-sand}$	Density of muddy sand
$\rho_{pack}$	Packing density of a sediment (mass of solids per unit volume)
$\rho_{qtz}$	Density of quartz
$\rho_0$	Density of water
$\rho_U, \rho_1$	Density of upper/lower layers in a bed
$\sigma$	Growth rate of instability
$\sigma_1$	Sorting coefficient
$\tau$	Bed shear stress
$\Theta$	Shields parameter
$\phi$	Porosity
$\phi_c, \phi_f$	Porosity of coarse sediment and fine sediment
$\phi_{MIN}$	Minimum porosity in a sediment mixture
$\phi_{CRIT}$	Critical porosity marking transition in grain support mechanism
$\Phi_f$	Volumetric fraction of fine material in the bed



## Appendix: Analysis of the Kelvin–Helmholtz instability between an inviscid and a viscous fluid

The overlying flow is modelled as infinitely deep, inviscid and irrotational, with constant unperturbed speed  $U$  in the  $x$ -direction. The underlying fluid is Newtonian and of high viscosity (i.e. it undergoes Stokes flow); it is also infinitely deep and is initially at rest. The unperturbed interface position is  $z = 0$ .

### Governing equations and boundary conditions

The upper layer obeys Laplace's equation and Bernoulli's equation:

$$\nabla^2 \phi = 0, \quad p = p_0 - \rho_1 \frac{\partial \phi}{\partial t} - \frac{1}{2} \rho_1 \left[ \left( U + \frac{\partial \phi}{\partial x} \right)^2 + \left( \frac{\partial \phi}{\partial z} \right)^2 \right] - \rho_1 g z. \quad (\text{A1})$$

Note that the velocity is:

$$\mathbf{u}_1 = U \mathbf{e}_x + \nabla \phi. \quad (\text{A2})$$

The lower layer obeys continuity and Stokes flow:

$$\nabla \cdot \mathbf{u}_2 = 0, \quad \nabla^2 \mathbf{u}_2 = \nabla p_2 + \rho_2 g \mathbf{e}_z. \quad (\text{A3})$$

At the interface  $z = \eta(x, t)$ , the flows satisfy the kinematic conditions:

$$\frac{\partial \eta}{\partial t} + \left( U + \frac{\partial \phi}{\partial x} \right) \frac{\partial \eta}{\partial x} = \frac{\partial \phi}{\partial z}, \quad \frac{\partial \eta}{\partial t} + u_2 \frac{\partial \eta}{\partial x} = w_2, \quad (\text{A4})$$

along with the stress and pressure continuity conditions:

$$p_1 = p_2, \quad \boldsymbol{\tau}_2 = \mathbf{0}, \quad (\text{A5})$$

where  $\boldsymbol{\tau}_2$  is the tangential shear stress on the interface.

Finally, the far-field conditions are:

$$\phi \rightarrow 0, p_1 \sim p_0 - \rho_1 g z \text{ as } z \rightarrow \infty; \quad \mathbf{u}_2 \rightarrow \mathbf{0}, p_2 \sim p_0 - \rho_2 g z \text{ as } z \rightarrow -\infty. \quad (\text{A6})$$

## Linearisation

Seeking normal-mode solutions of the form:

$$\begin{aligned} \eta &= \varepsilon \eta_0 e^{ikx} e^{\sigma t}, \quad \phi = \varepsilon \Phi(z) e^{ikx} e^{\sigma t}, \quad p_1 = \varepsilon P_1(z) e^{ikx} e^{\sigma t}, \\ p_2 &= \varepsilon P_2(z) e^{ikx} e^{\sigma t}, \quad u_2 = \varepsilon U(z) e^{ikx} e^{\sigma t}, \quad w_2 = \varepsilon W(z) e^{ikx} e^{\sigma t}, \end{aligned} \quad (\text{A7})$$

the governing equations at  $\mathcal{O}(\varepsilon)$  become:

$$\begin{aligned} -k^2 \Phi + \frac{d^2 \Phi}{dz^2} = 0, \quad P_1(z) + \rho_1 U \Phi k i + \rho_1 \phi \sigma = 0, \quad -\mu_2 U k^2 + \mu_2 \frac{d^2 U}{dz^2} - i P_2 k = 0, \\ -\mu_2 W k^2 + \mu_2 \frac{d^2 W}{dz^2} - \frac{d P_2}{dz} = 0, \quad U k i + \frac{d W}{dz} = 0. \end{aligned} \quad (\text{A8})$$

Solving in each region, applying the far-field boundary conditions and normalising the amplitude of  $\phi$  to unity yields:

$$P_1(z) = -(\rho_1 U k i + \rho_1 \sigma) e^{-kz}, \quad \Phi(z) = e^{-kz} \quad (\text{A9})$$

and:

$$\begin{aligned} P_2(z) = 2C_2 \mu_2 e^{kz}, \quad U(z) = \frac{(C_1 k e^{kz} + C_2 k e^{kz} z + C_2 e^{kz}) i}{k}, \\ W(z) = C_1 e^{kz} + C_2 e^{kz} z, \end{aligned} \quad (\text{A10})$$

where  $C_1$  and  $C_2$  are as yet undetermined constants.

The linearised interface boundary conditions at  $z = 0$  become:

$$p_2 + \eta \frac{\partial p_2}{\partial z} = p_1 + \eta \frac{\partial p_1}{\partial z}, \quad \frac{\partial \eta}{\partial t} + U \frac{\partial \eta}{\partial x} = \frac{\partial \phi}{\partial z}, \quad \frac{\partial \eta}{\partial t} = w_2, \quad \frac{\partial u_2}{\partial x} = 0. \quad (\text{A11})$$

These yield the system:

$$\begin{aligned} 2\mu_2 C_2 - \eta_0 \rho_2 g + \rho_1 U k i + \rho_1 \sigma + \eta_0 \rho_1 g = 0, \quad \eta_0 \sigma + \eta_0 k U i + k = 0, \\ \eta_0 \sigma - C_1 = 0, \quad -C_1 k - C_2 = 0, \end{aligned} \quad (\text{A12})$$

which reduces to:

$$\eta_0 = -\frac{k}{\sigma + k U i}, \quad C_1 = \eta_0 \sigma, \quad C_2 = -\eta_0 \sigma k \quad (\text{A13})$$

and:

$$-\frac{k}{\sigma + k U i} (-2\mu_2 \sigma k - g(\rho_2 - \rho_1)) + \rho_1 U k i + \rho_1 \sigma = 0. \quad (\text{A14})$$

Hence the dispersion relation as a quadratic as obtained:

$$\Sigma^2 + 2(i\kappa + M\kappa^2)\Sigma + \kappa - \kappa^2 = 0, \quad (\text{A15})$$

where the dimensionless variables are:

$$\sigma = \frac{g'}{U}\Sigma, \quad k = \frac{g'}{U^2}\kappa, \quad g' = \left(\frac{\rho_2}{\rho_1} - 1\right), \quad \text{and} \quad M = \frac{\mu_2}{\rho_1} \frac{g'}{U^3}. \quad (\text{A16})$$

The parameter  $M$  measures the relative importance of viscous to inertial-gravity effects.

The solutions for  $\Sigma$  are easily obtained as:

$$\Sigma = \Sigma_{\pm} = -i\kappa - M\kappa^2 \pm (2i\kappa^3 M + M^2\kappa^4 - \kappa)^{\frac{1}{2}}. \quad (\text{A17})$$

The dominant solution is  $\Sigma_+$ . It is easy to show that  $\Re(\Sigma_+)$  is negative for  $0 < \kappa < 1$ , passes through zero at  $\kappa = 1$  and monotonically increases towards a finite value:

$$\Re(\Sigma_+) \rightarrow \frac{1}{2M} \quad \text{as} \quad \kappa \rightarrow \infty. \quad (\text{A18})$$

In dimensional terms, this means that the growth rate of perturbations is bounded above by:

$$\sigma_{\max} = \frac{1}{2} \frac{g'}{U} \frac{1}{M} = \frac{\rho_1 U^2}{2\mu_2}. \quad (\text{A19})$$

Note, finally, that in the limit  $\kappa \rightarrow \infty$  the model becomes inadequate, both because short waves will 'see' the non-sharpness of the change in velocity at the interface, and because when  $k\varepsilon \sim 1$  the assumption of gentle variation behind the linearised model breaks down. Formally, this is the limiting growth rate for very short waves. In fact, the model is expected to break down for waves shorter than the boundary-layer thickness associated with the overlying flow, so if instability is predicted only for very short waves then it is possible that in fact it will not occur at all.

## TABLES

**Table 1**

Physical parameter	Notation	Minimum	Maximum	Units	Origin
Grain size	$d$	$10^{-5}$ (10 $\mu\text{m}$ )	$10^{-4}$ (100 $\mu\text{m}$ )	m	Measured
Bed thickness	$h$	$5 \times 10^{-2}$	$5 \times 10^{-2}$	m	Measured
Bed density	$\rho_{bed}$	$1.8 \times 10^3$	$2.2 \times 10^3$	$\text{kg m}^{-3}$	Estimated
Suspension vol fraction	$\varphi$	0.05	0.1		Estimated
Bed vol fraction	$\eta$	0.5	0.7		Estimated
Shields parameter	$\Theta$	0.03	1		Estimated
Settling speed	$w_s$	$10^{-4}$	$10^{-3}$	$\text{m s}^{-1}$	Inferred
Deposition time	$T_{dep}(w_s)$	300	6000	s	Inferred
Bed shear stress	$\tau(\Theta)$	0.015	0.5	Pa	Inferred
Current speed	$U(\Theta)$	0.04	0.5	$\text{m s}^{-1}$	Inferred
Bed viscosity	$\mu(\Theta, w_s)$	4.5	300	Pa s	Inferred

**Table 2**

Division	$d_{vol}$	$\Phi_f <$		
		32 $\mu\text{m}$	16 $\mu\text{m}$	8 $\mu\text{m}$
Laminated silt, Bouma D	50 $\mu\text{m}$	~ 50%	~ 40%	~ 20%
Convolute lamination	80 $\mu\text{m}$	~ 25%	~ 10%	~ 5%
Cross-laminated sand, Bouma C	100 $\mu\text{m}$	~ 10%	~ 5%	~ 2.5%

**TABLE CAPTIONS**

**Table 1:** Summary of the reconstructed physical parameter values and some of the interdependencies between inferred parameters, listed in order of increasing levels of uncertainty. A single representative bed thickness  $h$  is considered. Estimates are based principally on data from the Aberystwyth Grits, supplemented with the Icod turbidite data which are broadly similar.

**Table 2:** Summary of approximate grain-size data from core 166/27, listing the average volumetric grain size,  $d_{vol}$ , and  $\Phi_f$ , the fine fraction percentage above, below and within the convoluted region, for different arbitrary fine fraction upper boundaries.

**FIGURE CAPTIONS**

**Fig. 1.** Convolute lamination in two sandstone–mudstone turbidite beds (3 and 7) in the Trefechan Formation, Aberystwyth Grits (First Cove, Aberystwyth, SN 5828 8270). In both examples, the folds are confined to the sand-rich portion of the bed, and are bounded by cross-lamination below and planar lamination above.

**Fig. 2.** (A) Characteristics of ‘convolute bedding’ in the Aberystwyth Grits as defined by Kuenen (1953). (B) Kinematic classification of convolute lamination based on truncation of laminae (Allen, 1977; 1985).

**Fig. 3.** Proposed formation mechanisms for convolute lamination: (A) downslope shear (e.g. Rich, 1950; Dżułyński *et al.*, 1959); (B) current shear (e.g. Keunen, 1953; Ten Haaf, 1956); (C) buoyancy instability (e.g. Natland & Keunen, 1951, Dżułyński & Smith, 1963; Allen, 1977); (D) water escape (e.g. Migliorini, 1950).

**Fig. 4.** Geological map of the Aberystwyth Grits, with dominant palaeoflow directions and main localities studied.

**Fig. 5.** Optical scans of polished surfaces through convolute lamination with line drawings of notable geometric features (Allt Wen, SN 576 797).

**Fig. 6.** A back-scattered image through convolute lamination: graded laminations are picked out by alternating zones of detrital quartz and chlorite-mica stacks, the altered product of mud.

**Fig. 7.** (A) Polished slab with (B) thin-sections taken through the convoluted region and (C) a series of microscope photographs. These suggest that the sand is relatively clean below the convoluted zone (*ii* and *ii*) with increasing silt/mud and chlorite-mica stacks moving upward through the convolutions (*iii* and *iv*). Above the convolutions, sand is absent (*v*).

**Fig. 8.** Extent of Icod debris avalanche and turbidite, a volcanoclastic event originating from Tenerife (from Hunt *et al.* 2011). The series of cores presented are taken through the centre of the Agadir Basin (AB) with the grain-size data taken from CD166-27.

**Fig. 9.** A schematic of core 166/27 (Hunt *et al.*, 2011). Seven subunits are identified by Hunt *et al.* (2011). These relate to the order of retrogressive failure of the source area. Convolute lamination is present in subunits 2 and 3.

**Fig. 10.** Photographs of four cores through the Icod turbidite (Bed 14), taken tens of kilometres apart along the axis of the Agadir Basin, showing the lowermost subunits and the folding present in subunits 2 and 3.

**Fig. 11.** In (A), grain-size measurements with deposit height through core 166/27 are presented using four different measures for average grain size: volumetric mean,  $d_{vol}$ , modal value,  $d_{mode}$ , 50<sup>th</sup> percentile ( $d_{50}$ ) and 90<sup>th</sup> percentile ( $d_{90}$ ). Each subunit fines upward. Shaded areas mark regions of convolute lamination; dashed lines mark boundaries between subunits representing different stages of retrogressive failure. In (B), the proportion of sediment less than 32  $\mu\text{m}$  ( $5\phi$ ) increases with height through the convolutions, and markedly within the sediment overlying the convolutions.

**Fig. 12.** A plot of the proportion of fine sediment,  $\Phi_F$ , against average grain size,  $d_{vol}$ , coded by sedimentary structure, reveals a window within which convolute lamination occurs. Planar laminated sand (Bouma B) and cross-laminated sand (Bouma C) is coarser and fines-poor; overlying laminated silt (Bouma D/E) is usually finer with a significantly higher proportion of fines.

**Fig. 13.** Grain-size distribution curves for three samples taken at different heights within the convolute lamination of subunit 2 (base, middle, top) from Icod core CD166/27. Additional samples from underlying cross-laminated sand and overlying silt provide lower and upper bounds. Data was output in bins of constant width of  $\frac{1}{4}\phi$ . Grain size is thus plotted on the  $\phi$  log scale, so that the area under each sample curve remains constant.

**Fig. 14.** Plots of sorting,  $\sigma_I$ , (Folk & Ward, 1957) with (A) bed height, (B) proportion of fines,  $\Phi_F$ . Cross-laminated sand below the convolutions in both subunits is better sorted than the convoluted layer, owing to the lack of fines. Laminated silt above is more poorly sorted, due to the significant proportion of fine silt (c.f. Fig. 7A). Convoluted sediment lies in between. Sorting correlates well with fines content ( $r = 0.95$ ).

**Fig. 15.** Relationship between skewness and proportion of fines  $\Phi_F$  with the different divisions plotting in different regions of parameter space.

**Fig. 16.** Definition diagrams for parameters used in the quantitative analyses of convolute lamination formation mechanisms.

**Fig. 17.** Three illustrations show the relations between porosity, bed density and grain size based on experiments and numerics: (A) Experiments on bidisperse mixtures of ca 280  $\mu\text{m}$  sand and <4  $\mu\text{m}$  clay by Marion *et al.* (1992) identify a porosity minimum that is lower than the porosities of either pure end-member. (B) Explanation for a porosity minimum and corresponding density maximum in

terms of a coarse-packing and fine-packing transition (from Koltermann & Gorelick (1995). (C) Exploring the role of the ratio of grain sizes on porosity of a bimodal mixtures (from Brouwers, 2006).

**Fig. 18:** Schematic diagram through a fine-grained graded turbidite containing convolute lamination, based on field observations and core measurements. Detrital sand gently grades normally through Bouma B and C divisions, and the convolutions, while the proportion of fines increases more markedly. The laminated silt above the folds is noticeably finer-grained. Grain size and sorting are measured; bed density is inferred.

**Fig. 19:** Summary diagram of the formation of convolute lamination in the Aberystwyth Grits. Deposition of rippled sediment (1) from the flow forms the linguoid substrate upon which the folds nucleate. Buoyancy-instability develops (2) owing to an unstable density gradient within the forming bed. The resulting folds are sheared and amplified by the overriding, still-depositing current (3). Deposition of the finest sediment from the flow suppresses further development of the folds (4).

## REFERENCES

- Allen, J.R.L.** (1977) The possible mechanics of convolute lamination in graded sand beds. *Journal of the Geological Society*, **134**, 19-31.
- Allen, J.R.L.** (1985) *Principles of physical sedimentology*. George Allen & Unwin, London, 272 pp.
- Amy, L.A., Talling, P.J., Edmonds, V.O., Sumner, E.J. and Lesueur, A.** (2006) An experimental investigation of sand–mud suspension settling behaviour: implications for bimodal mud contents of submarine flow deposits. *Sedimentology* **53**, 1411–1434.
- Anketell, J.M., Cegla, J. and Dżułyński, S.** (1970) On the deformational structures in systems with reverse density gradients. *Annales de la Société Géologique de Pologne*, **40**, 3-29.
- Anketell, J.M. and Dżułyński, S.** (1968) Patterns of density-controlled convolutions involving statistically homogeneous and heterogeneous layers. *Annales de la Société Géologique de Pologne*, **38**, 401-409.
- Anketell, J.M. and Lovell, J.P.B.** (1976) Upper Llandoveryian Grogal Sandstones and Aberystwyth Grits in the New Quay area, Central Wales: a possible upwards transition from contourites to turbidites. *Geological Journal*, **11**, 101-108.



- Arya, L.M. and Paris, J.F.** (1981) A physicoempirical model to predict the soil moisture characteristic from particle-size distribution and bulk density data. *Soil Science Society of America Journal*, **45**, 1023-1030.
- Avseth, P.** (2010) Explorational rock physics: the link between geological processes and geophysical observables. In: (ed: K. Bjorlykke) *Petroleum Geoscience: from sedimentary environments to rock physics*, 2<sup>nd</sup> edition, Springer.
- Bailey, E.B.** (1930) New light on sedimentation and tectonics. *Geological Magazine*, **67**, 77-92.
- Baas, J.H., Best, J.L. and Peakall, J.** (2015) Predicting bedforms and primary current stratification in cohesive mixtures of mud and sand. *Journal of the Geological Society*, **173**, 12-45.
- Benjamin, T.B. and Mullin, T.** (1988) Buckling instabilities in layers of viscous liquid subjected to shearing. *Journal of Fluid Mechanics*, **195**, 523-540.
- Brouwers, H.J.H.** (2006) Particle-size distribution and packing fraction of geometric random packings. *Physical Review E*, **74**, 031309.
- Butler, R.W.H., Eggenhuisen, J.T., Haughton, P. and McCaffrey, W.D.** (2016) Interpreting syndepositional sediment remobilization and deformation beneath submarine gravity flows; a kinematic boundary layer approach. *Journal of the Geological Society*, **173**, 46-58.
- Challinor, J.** (1949) The origin of certain rock structures near Aberystwyth. *Proceedings of the Geologists' Association*, **60**, 48-53.
- Chandrasekar, S.** (1961) *Hydrodynamic and hydrodynamic stability*. Oxford University Press, Oxford, 652 pp.
- Cherns, L., Cocks, L.R.M., Davies, J.R., Hillier, R.D., Waters, R.A. and Williams, M.** (2006) Silurian: the influence of extensional tectonics and sea-level changes on sedimentation in the Welsh Basin and on the Midland Platform. In: *The geology of England and Wales* (Eds P.J. Brenchley and P.F. Rawson), pp. 75-102. Geological Society of London.
- Conrad, C.P. and Molnar, P.** (1997) The growth of Rayleigh–Taylor-type instabilities in the lithosphere for various rheological and density structures. *Geophysical Journal International*, **129**, 95–112.
- Cumberland, D.J. and Crawford, R.J.** (1987) *The packing of particles*. Handbook of Powder Technology, vol. 6. Elsevier, Amsterdam, 150 pp.
- Davies, J.R., Fletcher, C.J.N., Waters, R.A., Wilson, D., Woodhall, D.G. and Zalasiewicz, J.A.** (1997) *Geology of the country around Llanilar and Rhayader*. Memoir, British Geological Survey, Sheets 178 & 179 (England & Wales), Nottingham, 267 pp.
- Dimberline, A. J.** (1986) Electron microscope and microprobe analysis of chlorite-mica stacks in the Wenlock turbidity, mid Wales, U.K. *Geological Magazine*, **123**, 299-306.

- Dott, R.H.** and **Howard, J.K.** (1962) Convolute lamination in non-graded sequences. *Journal of Geology*, **70**, 114-121.
- Drazin, P.G.** (2002) *Introduction to hydrodynamic instability*. Cambridge University Press, Cambridge, 258 pp.
- Dvorkin, J., Gutierrez, M.A.** and **Grana, D.** (2014) Seismic reflections of rock properties. Cambridge University Press, Cambridge, 324 pp.
- Dyer, K. R.** (1986) *Coastal and Estuarine Sediment Dynamics*. Wiley, Chichester, 358 pp.
- Dźułyński, S.** (1966) Sedimentary structures resulting from convection-like pattern of motion. *Annales de la Société Géologique de Pologne*, **36**, 3-21.
- Dźułyński, S., Książkiewicz, M.** and **Kuenen, P.H.** (1959) Turbidites in flysch of the Polish Carpathian Mountains. *Geological Society of America Bulletin*, **70**, 1089-1118.
- Dźułyński, S.** and **Smith, A.J.** (1963) Convolute lamination, its origin, preservation, and directional significance. *Journal of Sedimentary Petrology*, **33**, 616-627.
- Esselburn, J.D., Ritzi, R.W.** and **Dominic, D.F.** (2011) Porosity and permeability in ternary sediment mixtures. *Ground Water*, **49(3)**, 393–402.
- Fearnside, W.G.** (1910) The Tremadoc slates and associated rocks of Southeast Carnarvonshire. *Quarterly Journal of the Geological Society, London*, **66**, 142-188.
- Folk, R.L.** and **Ward, W.C.** (1957) Brazos River Bar: a study in the significance on grain size parameters. *Journal of Sedimentary Petrology*, **27**, 3-26.
- Frenz, M., Wynn, R.B., Georgiopoulou, A., Bender, V.B., Hough, G., Masson, D.G., Talling, P. J.** and **Cronin, B.T.** (2009) Provenance and pathways of later Quaternary turbidites in the deep-water Agadir Basin, northwest African margin. *International Journal of Earth Sciences*, **98**, 721-733.
- Frey, S.E., Gingras, M.K.** and **Dashtgard, S.E.** (2009) Experimental studies of gas-escape and water-escape structures: Mechanisms and morphologies. *Journal of Sedimentary Research*, **79**, 808-816.
- Furnas, C.C.** (1931) Grading Aggregates – 1. – Mathematical relations for beds of broken solids of maximum density. *Industrial and Engineering Chemistry*, **23**, 1052-1058.
- Ghanbarian-Alavijeh, B., Millan, H.,** and **Guanhua, H.** (2011) A review of fractal, prefractal and pore-solid-fractal models for parameterizing the soil water retention curve, *Canadian Journal of Soil Science*, **91(1)**, 1-14.

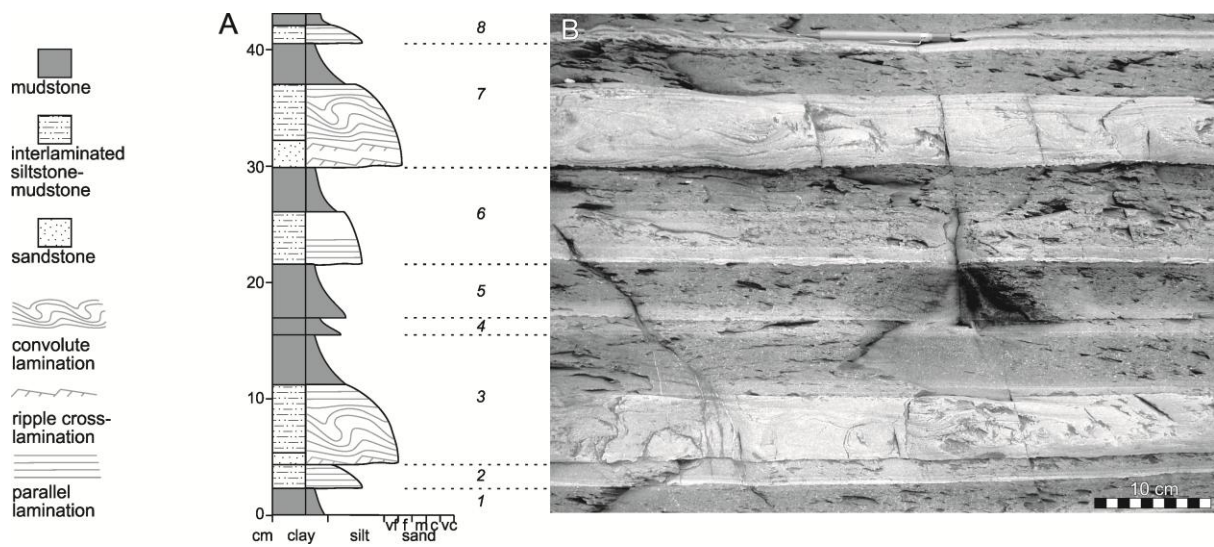
- Garcia, M. and Parker, G.** (1993) Experiments on the entrainment of sediment into suspension by a dense bottom current. *Journal of Geophysical Research*, **98(C3)**, 4793–4807.
- Holland, C.H.** (1959) On convolute bedding in the Lower Ludlovian rocks of north-east Radnorshire. *Geological Magazine*, **96**, 230-236.
- Hunt, J.E., Wynn, R.B., Masson, D.G., Talling, P.J. and Teagle, D.A.H.** (2011) Sedimentological and geochemical evidence for multistage failure of volcanic island landslides: A case study from Icod landslide on north Tenerife, Canary Islands. *Geochem. Geophys. Geosyst.*, **12**, Q12007, doi: 10.1029/2011GC003740.
- Jones, O.T.** (1938) On the evolution of a geosyncline. *Quarterly Journal of the Geological Society, London*, **94**, lx-cx.
- Jones, O.T. and Pugh, W.J.** (1935) The geology of the districts around Machynlleth and Aberystwyth. *Proceedings of the Geologists' Association*, **46**, 247-300.
- Kamann, P.J., Ritzi, R.W., Dominic, D.F. and Conrad, C.M.** (2007) Porosity and permeability in sediment mixtures. *Ground Water*, **45(4)**, 429–438.
- Koltermann, C.E. and Gorelick, S.M.** (1995) Fractional packing model for hydraulic conductivity derived from sediment mixtures. *Water Resources Research*, **31(12)**, 3283-3297.
- Kneller, B. and Buckee, C.** (2000) The structure and fluid mechanics of turbidity currents: a review of some recent studies and their geological implications. *Sedimentology*, **47**, 62–94.
- Kuenen, P.H.** (1953) Graded bedding, with observations on Lower Paleozoic rocks of Britain. *Verhandelingen der Koninklijke Nederlandse Akademie van Wetenschappen*, **20**, 1-47.
- Kuenen, P.H. and Migliorini, C.I.** (1950) Turbidity currents as a cause of graded bedding. *Journal of Geology*, **58**, 91-127.
- Leeder, M. R.** (1982) *Sedimentology: Process and Product*. George Allen & Unwin, London, 344 pp.
- Lovell, J.P.B.** (1970) The palaeogeographical significance of lateral variations in the ratio of sandstone to shale and other features of the Aberystwyth Grits. *Geological Magazine*, **107**, 147-158.
- Marion, D., Nur, A., Yin, H, and Han, D.** (1987) Effects of porosity and clay content on wave velocities in sandstones, *Geophysics*, **51**, 2093-2107.
- Marion, D., Nur, A., Yin, H. and Han, D.** (1992) Compressional velocity and porosity in sand-clay mixtures. *Geophysics*, **57**, 554-563.

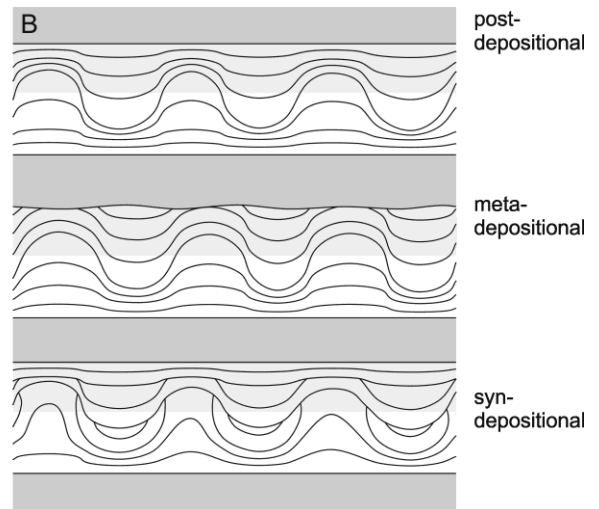
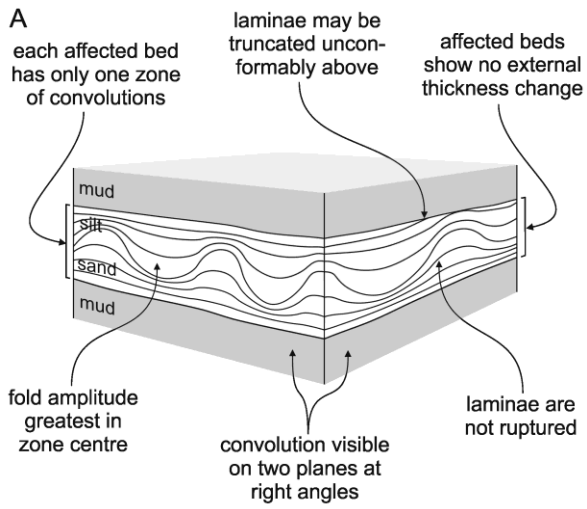
- McCann, T. and Pickering, K.T.** (1989) Palaeocurrent evidence of a northern structural high to the Welsh Basin during the Late Llandovery. *Journal of the Geological Society, London*, **146**, 211-212.
- McClelland, H.L.O., Woodcock, N.H. and Gladstone, C.** (2011) Eye and sheath folds in turbidite convolute lamination: Aberystwyth Grits Group, Wales. *Journal of Structural Geology*, **33**, 1140-1147.
- McGeary, R.K.** 1961. Mechanical packing of spherical particles. *Journal of American Ceramic Society*, **44**, 513-522.
- Mei, C.C., Liu, K.-F. and Yuhi, M.** (2001) Mud flow - slow and fast. In: *Geomorphological fluid mechanics* (Eds N. Balmforth and A. Provenzale), *Lecture Notes in Physics*, pp. 548-578. Springer-Verlag, Berlin.
- Merriman, R. J.** (2006) Clay mineral assemblages in British Lower Palaeozoic mudrocks. *Clay minerals*, **41**, 473-512.
- Middleton, G.V.** (1993) Sediment deposition from turbidity currents. *Annual Review of Earth and Planetary Sciences*, **21**, 89–114.
- Migliorini, C.I.** (1950) Dati a conferma della risedimentazione delle arenarie del macigno. *Atti della Società Toscana di Scienze Naturali, Memorie serie A*, **57**, 82-94.
- Mulder, T. and Alexander, J.** (2001) The physical character of subaqueous sedimentary density flows and their deposits. *Sedimentology*, **48**, 269-299.
- Nagtegaal, P.J.C.** (1963) Convolute lamination, metadepositional ruptures and slumping in an exposure near Pobla de Segur (Spain). *Geologie en Mijnbouw*, **42**, 363-374.
- Natland, M.L. and Kuenen, P.H.** (1951) Sedimentary history of the Ventura Basin, California, and the action of turbidity currents. *Special Publication of the Society of Economic Paleontologists and Mineralogists*, **2**, 76-107.
- Owen, G., Moretti, M. and Alfaro, P.** (2011). Recognising triggers for soft-sediment deformation: Current understanding and future directions. *Sedimentary Geology*. **235**, 133–140.
- Pirmez, C., Flood, R.D., Baptiste, J., Yin, H. and Manley, P.L.** (1997) Clay content, porosity and velocity of Amazon Fan sediments determined from ODP Leg 155 cores and wireline logs. *Geophysical Research Letters*, **24**, 317-320.
- Ramsey, J.G. and Huber, M.I.** (1987) *The techniques of modern structural geology Vol 2: Folds and Fractures*. Elsevier, Amsterdam, 392 pp.
- Rich, J.L.** (1950) Flow markings, groovings, and intra-stratal crumplings as criteria for recognition of slope deposits, with illustrations from Silurian rocks of Wales. *American Association of Petroleum Geologists Bulletin*, **34**, 717-741.

- Rogers, J.J. and Head, W.B.** (1961) Relationships between porosity, median size, and sorting coefficients of synthetic sands, *J. Sed. Pet.*, **31**, 467-470.
- Sanders, J.E.** (1960) Origin of convoluted laminae. *Geological Magazine*, **97**, 409-421.
- Sequeiros, O.E., Spinewine, B., Beaubouef, R.T., Sun, T., Garcia, M.H. and Parker, G.** (2010) Bedload transport and bed resistance associated with density and turbidity currents. *Sedimentology*, **57**, 1463–1490.
- Sohn, H,Y, and Moreland, C.** (1968) The effect of particle size distribution on packing density. *Canadian Journal of Chemical Engineering*, **46**, 162–167.
- Srivatsan, L., Lake, L.W. and Bonnezaze, R.T.** (2004) Scaling analysis of deposition from turbidity currents. *Geo-Marine Letters*, **24**, 63–74.
- Sullwold, H.H.** (1959) Nomenclature of load deformation in turbidites. *Geological Society of America Bulletin*, **70**, 1247-1248.
- Sullwold, H.H.** (1960) Load-cast terminology and origin of convolute bedding: some comments. *Geological Society of America Bulletin*, **71**, 635-636.
- Sumner, E.J., Talling, P.J, Amy, L. A., Wynn, R. B., Stephenson, C. J. and Frenz, M.** (2012) Facies architecture of individual basin-plain turbidites: Comparison with existing models and implications for flow processes. *Sedimentology*, **59**, 1850-1887.
- Sumner, E.J. and Paull, C.K.** (2014) Swept away by a turbidity current in Mendocino submarine canyon, California. *Geophysical Research Letters*, doi: 10.1002/2014GL061863.
- Stephenson, C.J., Talling, P.J., Masson, D.G., Sumner, E.J., Frenz, M. and Wynn, R.B.** (2014) The spatial and temporal distribution of grain-size breaks in turbidites. *Sedimentology*, **61**, 1120-1156.
- Ten Haaf, E.** (1956) Significance of convolute lamination. *Geologie en Mijnbouw*, **18**, 188-194.
- Yin, H, Nur, A. and Mavko, G.** (1993) Critical porosity – a physical boundary in poroelasticity. *International Journal of Rock Mechanics and Mining Sciences*, **30**(7), 805-808.
- Yu, A.B. and Standish, N.** (1987) Porosity calculations of multi-component mixtures of spherical particles. *Powder Technology*, **52**, 233–241.
- Visher, G.S. and Cunningham, R.D.** (1981) Convolute laminations -- a theoretical analysis: example of a Pennsylvanian sandstone. *Sedimentary Geology*, **28**, 175-188.
- Williams, E.** (1960) Intra-stratal flow and convolute folding. *Geological Magazine*, **97**.
- Wilson, D., Davies, J.R., Waters, R.A. and Zalasiewicz, J.A.** (1992) A fault-controlled depositional model for the Aberystwyth Grits turbidite system. *Geological Magazine*, **129**, 595-607.

**Wynn, R.B., Weaver, P.P.E., Stow, D.A.V. and Masson, D.J.** (2002) Turbidite depositional architecture across three interconnected deep-water basins on the northwest African margin. *Sedimentology*, **49**, 669-695.

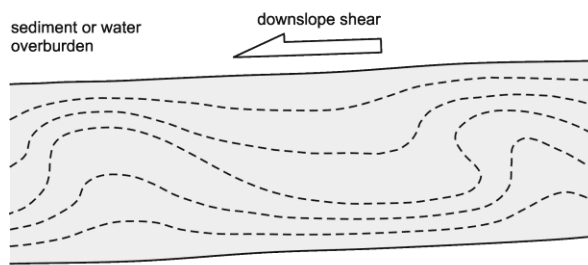
**Wood, A. and Smith, A.J.** (1958) The sedimentation and sedimentary history of the Aberystwyth Grits (Upper Llandoveryan). *Quarterly Journal of the Geological Society*, **114**, 163-195.



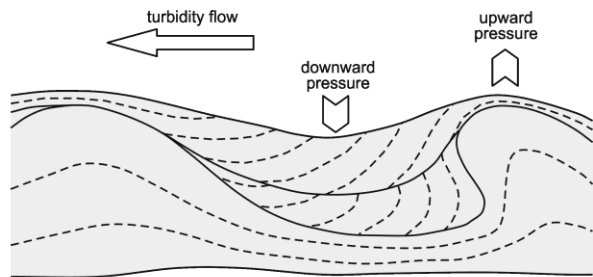




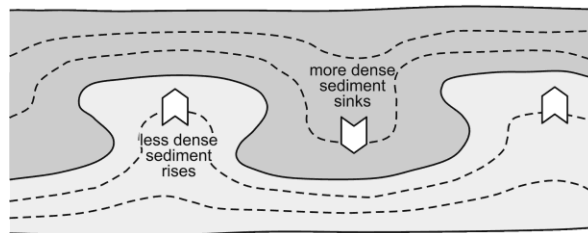
A post-depositional downslope shear



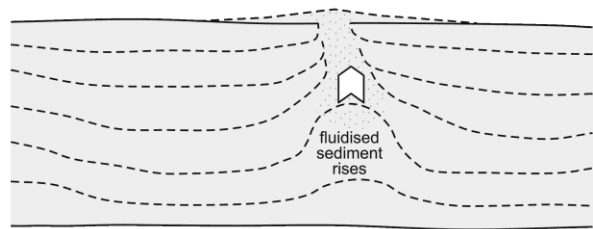
B syn-depositional current shear

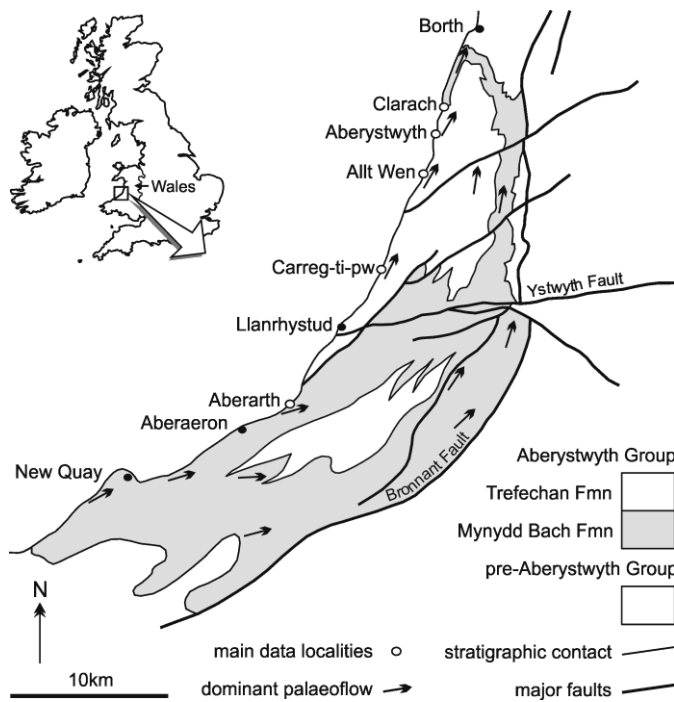


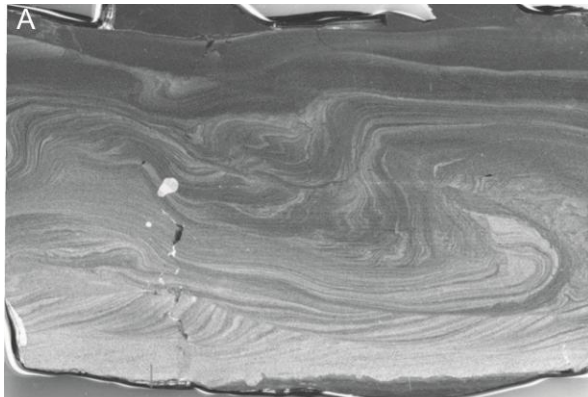
C buoyancy instability



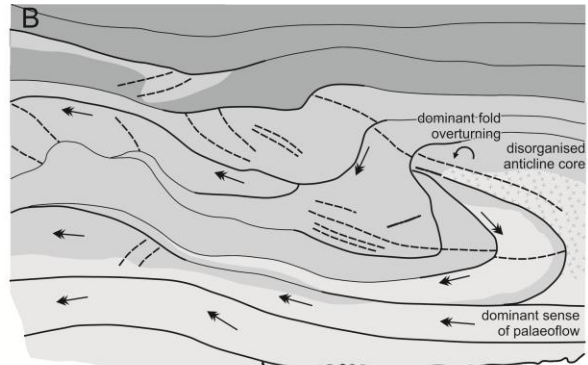
D water escape



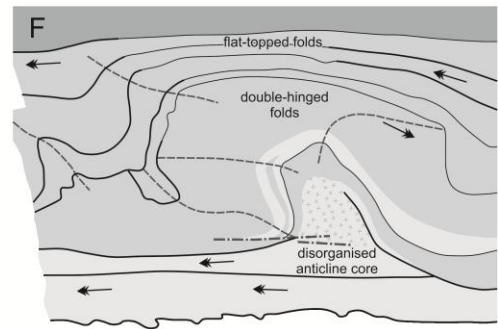
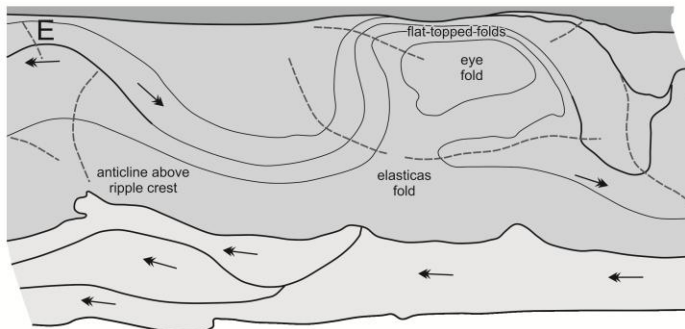
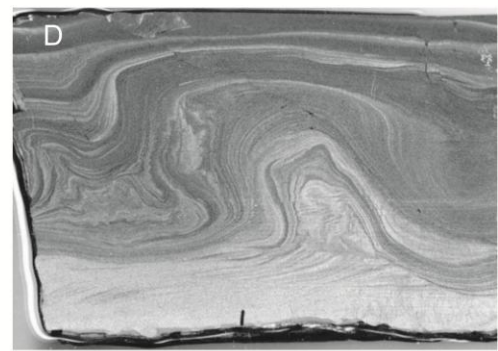
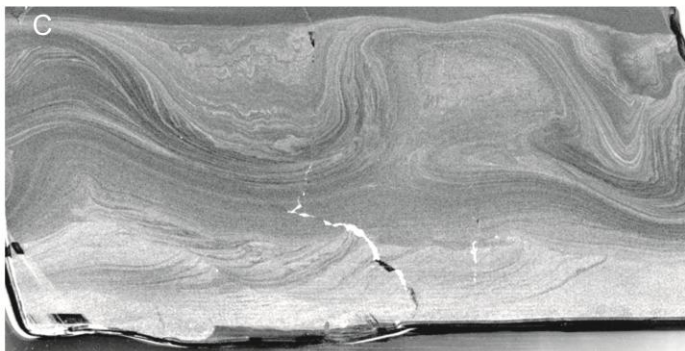


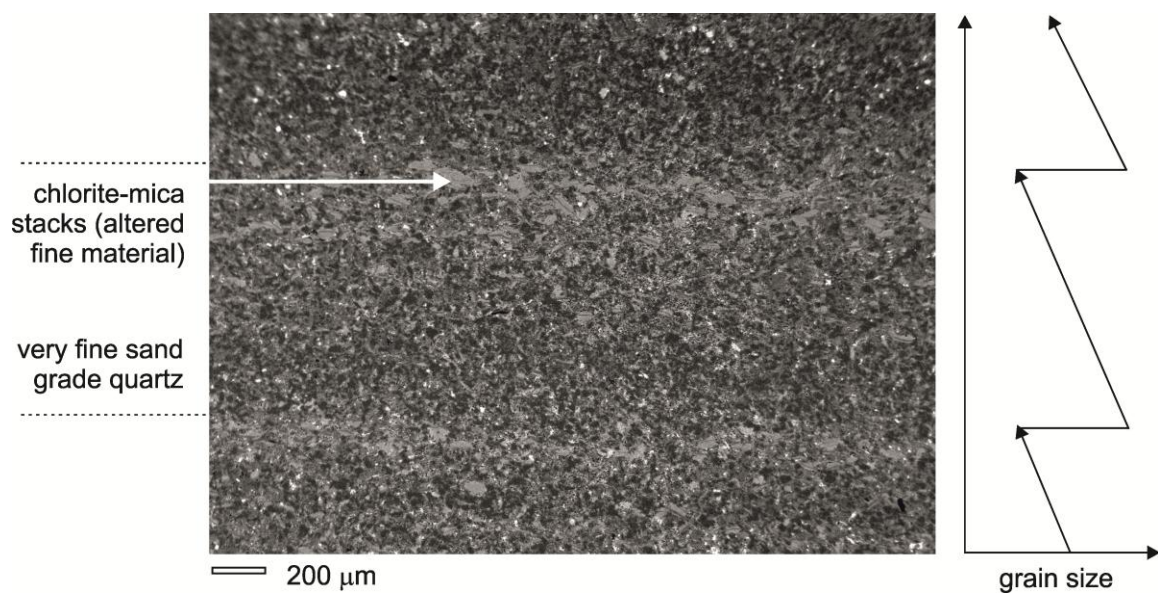


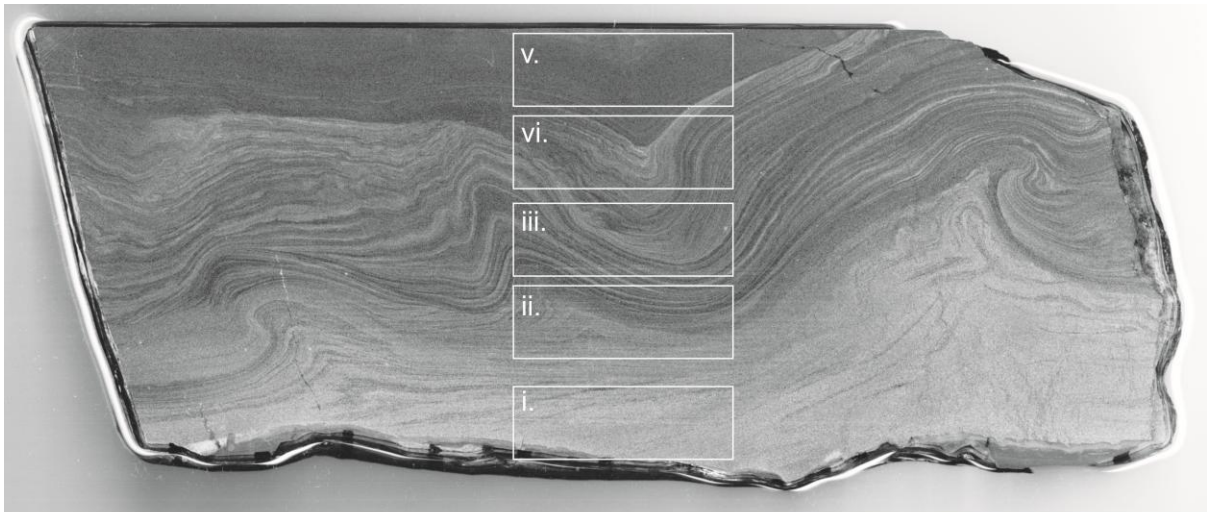
10 centimetres



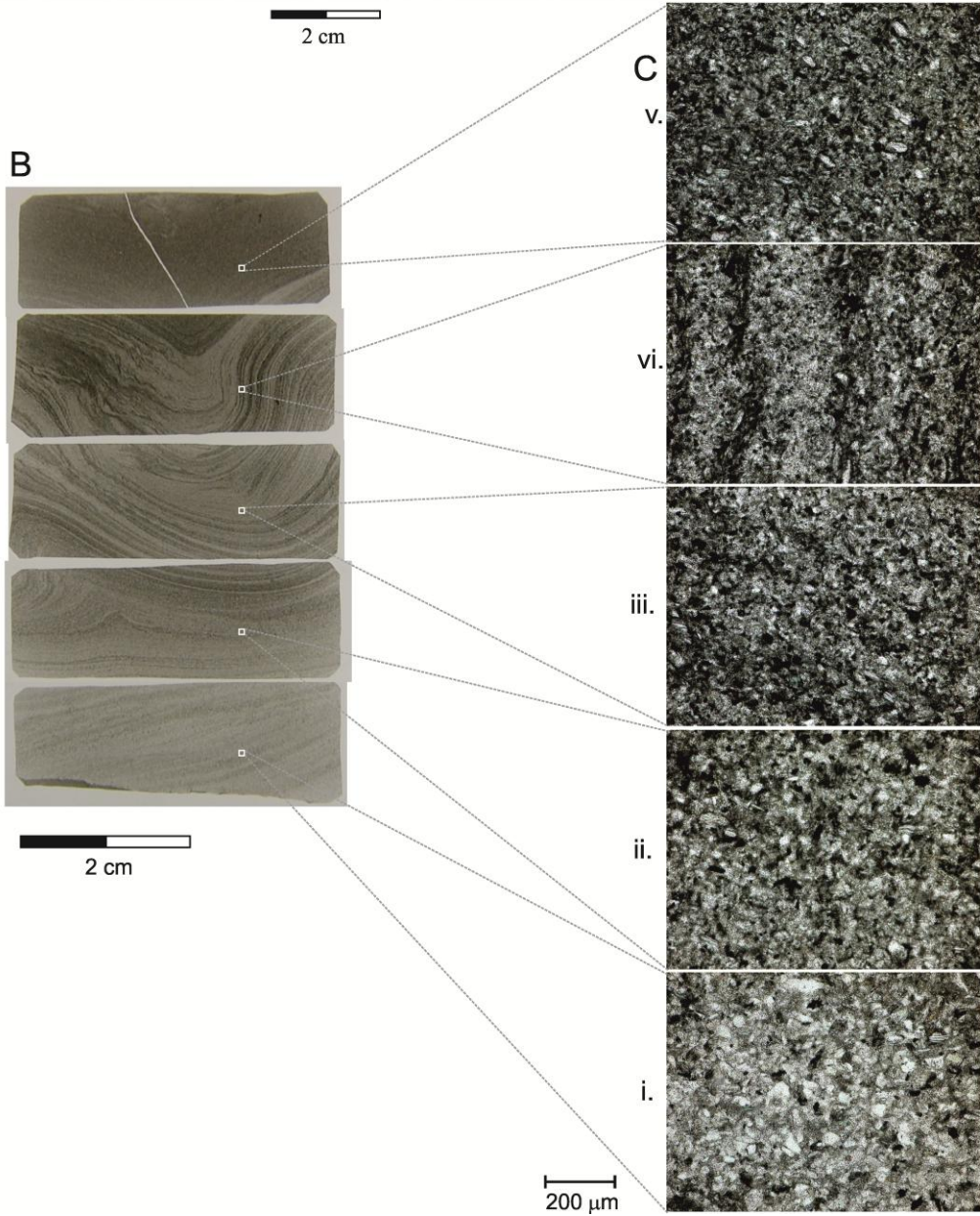
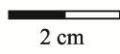
- mud
- interlaminated silt and clay
- very fine sand and silt
- disorganised sand
- discordant lamination surfaces
- concordant lamination surfaces
- fold axial surfaces
- shear surfaces
- apparent palaeoflow from cross-lamination sets

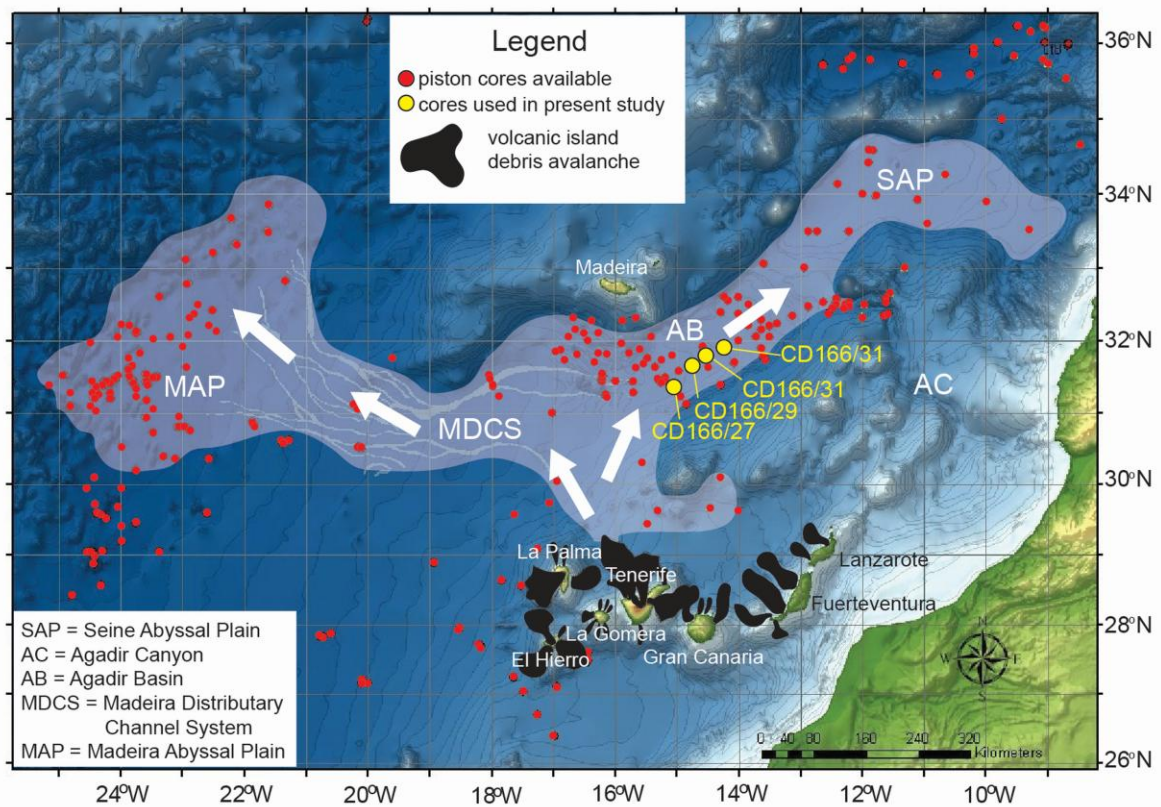


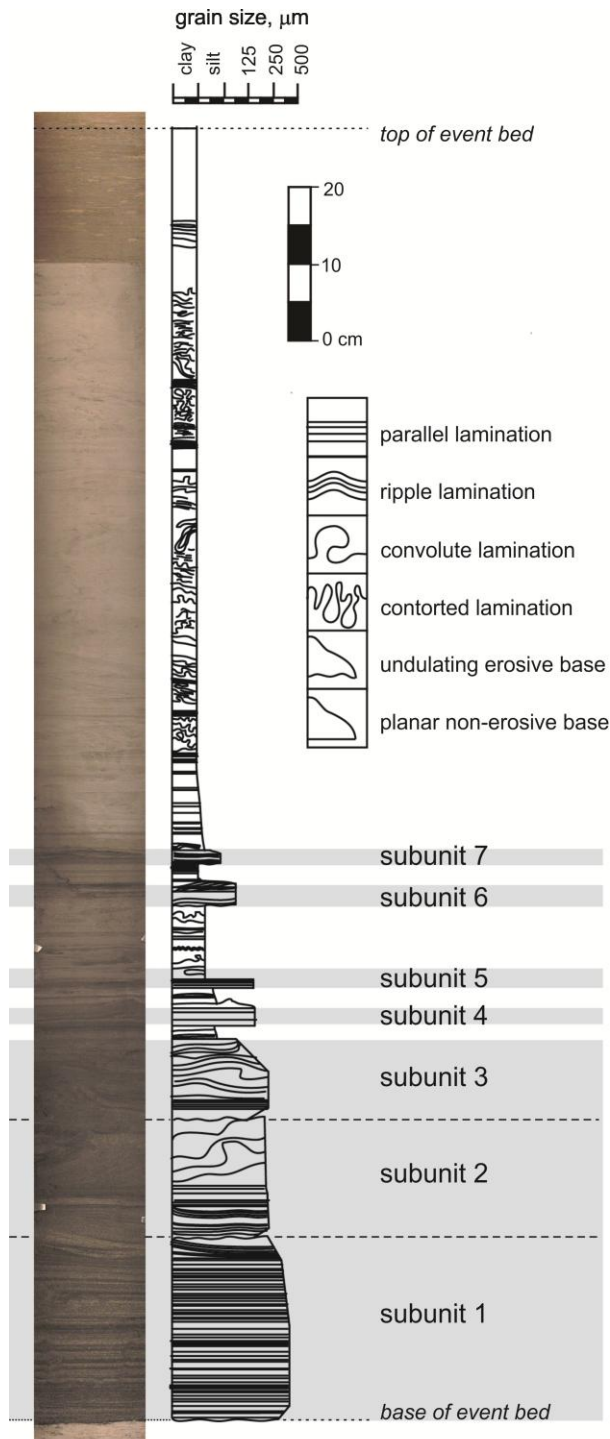


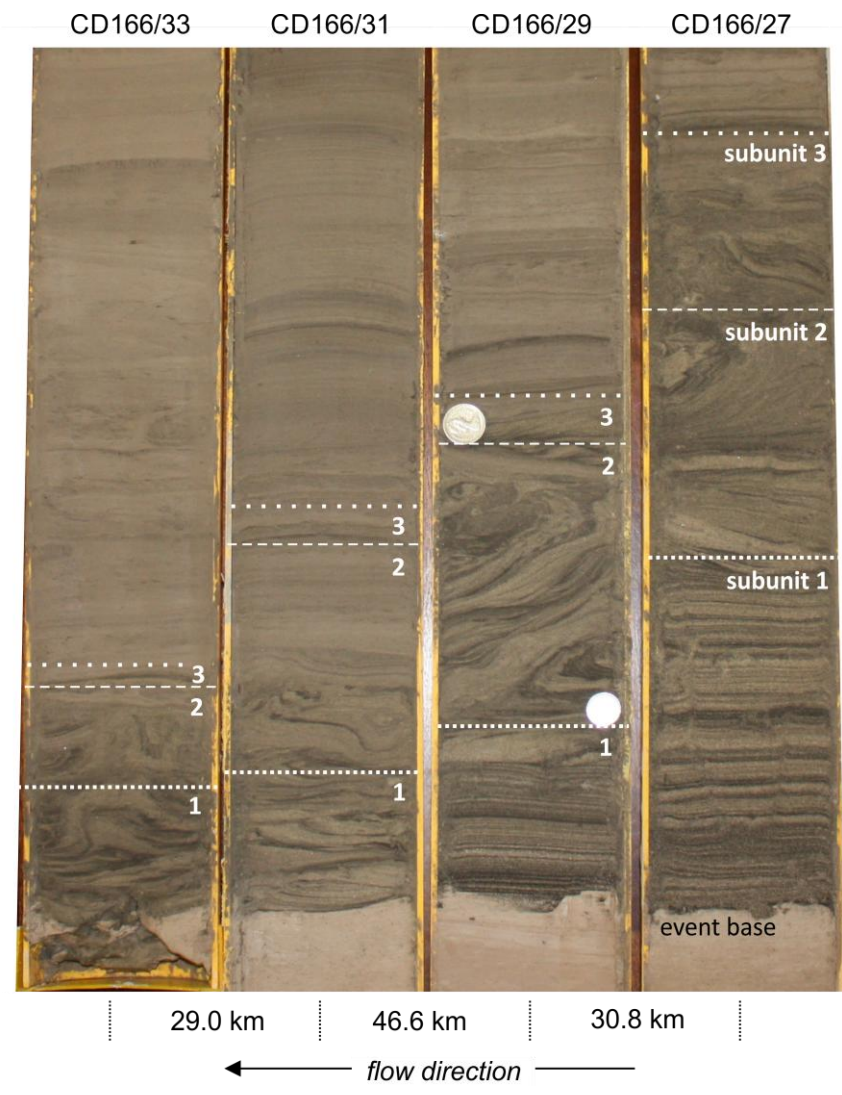


A

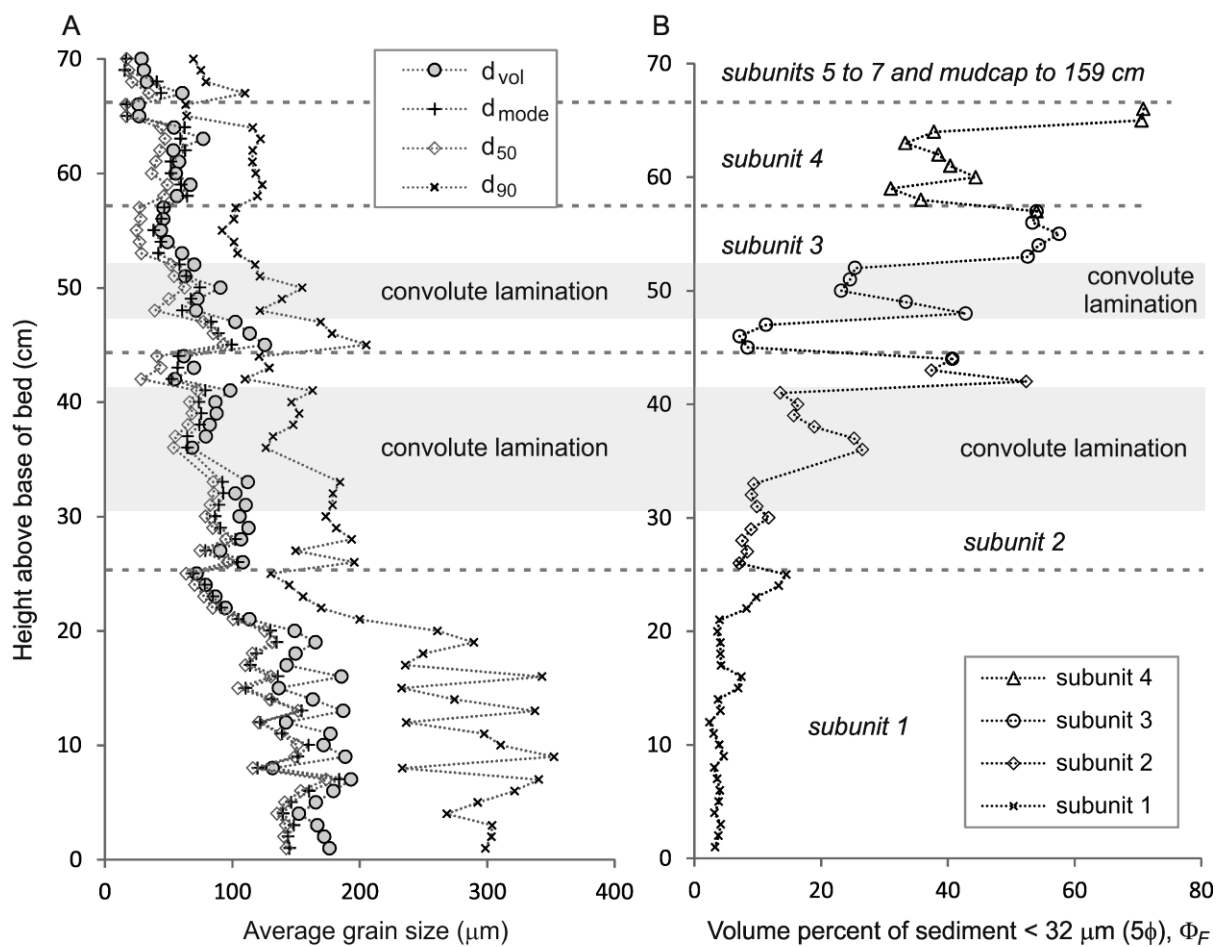


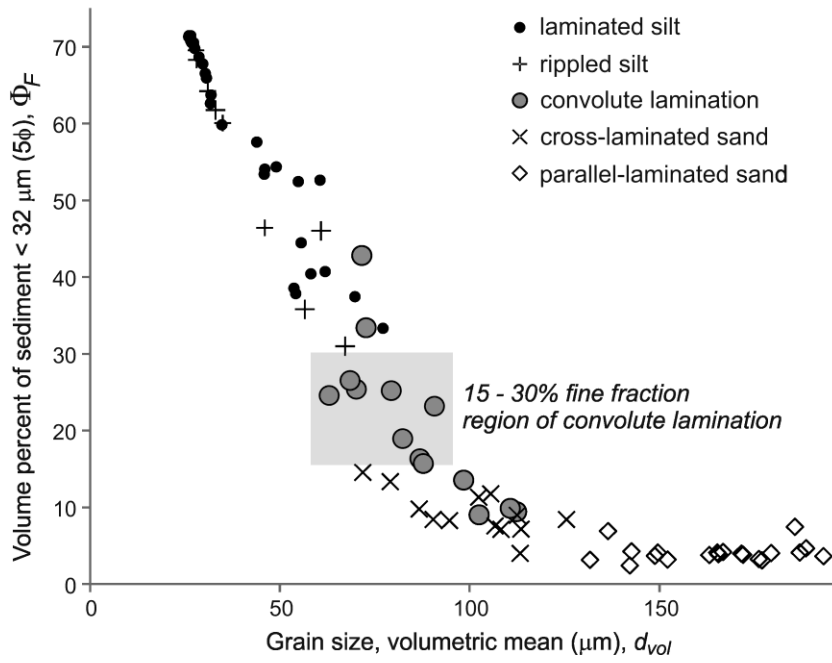


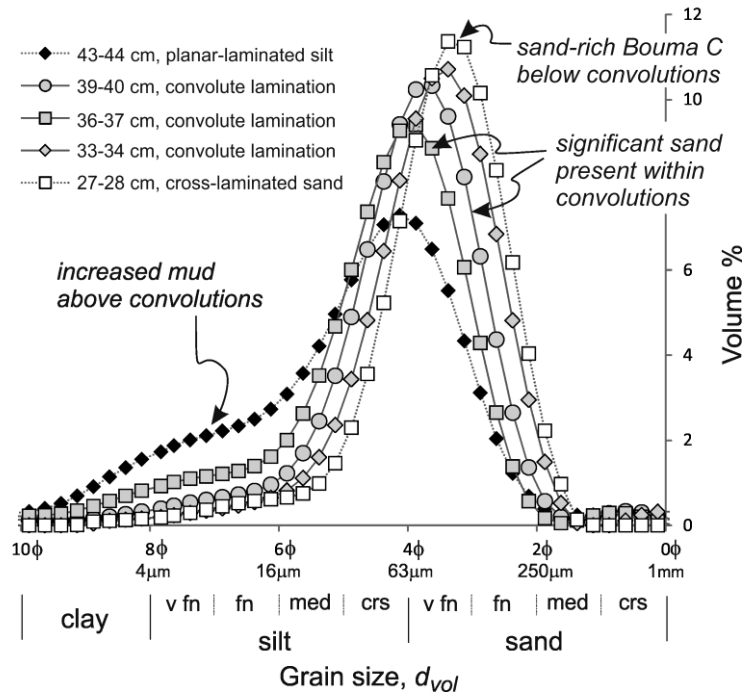


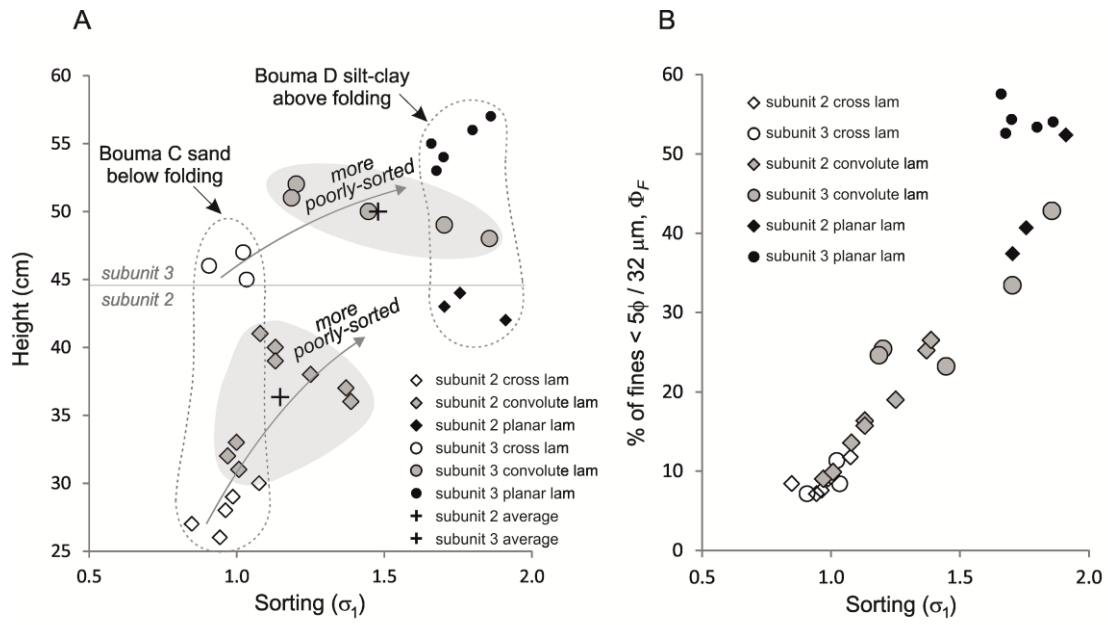


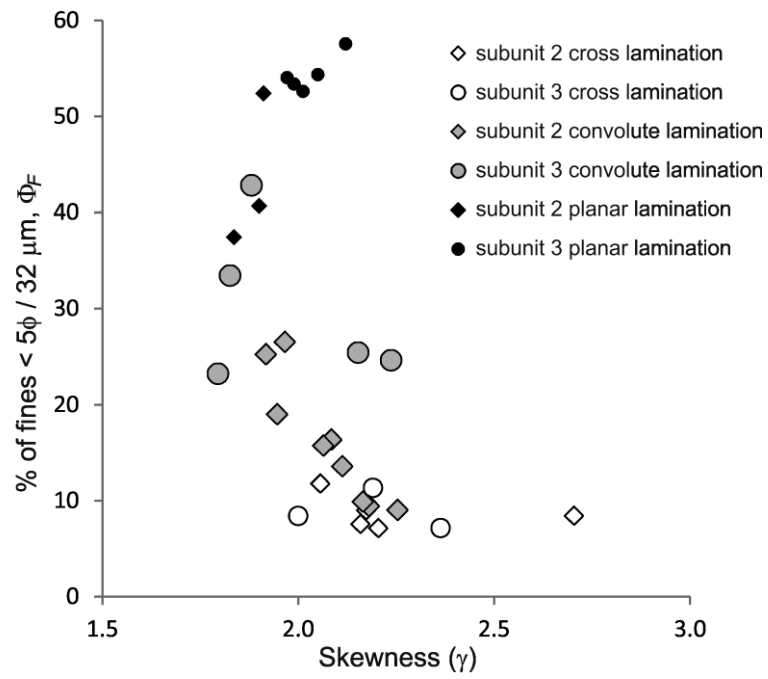




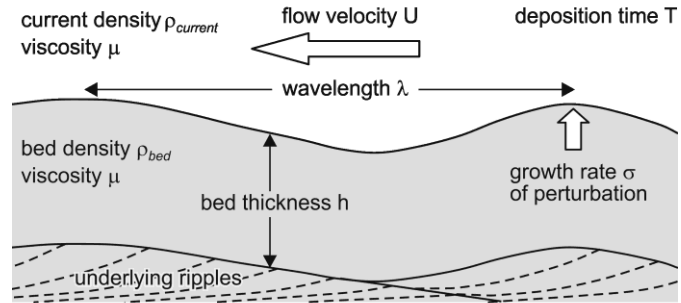




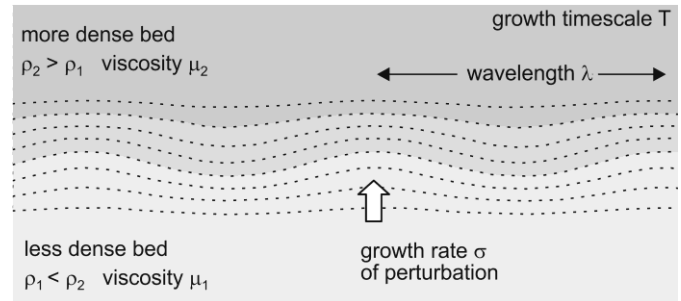




**A Kelvin-Helmholtz instability**



**B Rayleigh-Taylor instability**



**C viscous buckling instability**

